Fraunhofer Institut
Techno- und
Wirtschaftsmathematik

D. d'Humières, I. Ginzburg

Multi-reflection boundary conditions for lattice Boltzmann models

Berichte des Fraunhofer ITWM, Nr. 38 (2002)

ISSN 1434-9973

Bericht 38 (2002)

Die Veröffentlichungen in der Berichtsreihe des Fraunhofer ITWM können bezogen werden über:

Fraunhofer-Institut für Techno- und
Wirtschaftsmathematik ITWM
Gottlieb-Daimler-Straße, Geb. 49

67663 Kaiserslautern

Telefon: +49 (0) 6 31/2 05-32 42
Telefax: +49 (0) 6 31/2 05-41 39
E-Mail: info@itwm.fraunhofer.de
Internet: www.itwm.fraunhofer.de

Vorwort

Das Tätigkeitsfeld des Fraunhofer Instituts für Techno- und Wirtschaftsmathematik ITWM umfasst anwendungsnahe Grundlagenforschung, angewandte Forschung sowie Beratung und kundenspezifische Lösungen auf allen Gebieten, die für Techno- und Wirtschaftsmathematik bedeutsam sind.

In der Reihe »Berichte des Fraunhofer ITWM« soll die Arbeit des Instituts kontinuierlich einer interessierten Öffentlichkeit in Industrie, Wirtschaft und Wissenschaft vorgestellt werden. Durch die enge Verzahnung mit dem Fachbereich Mathematik der Universität Kaiserslautern sowie durch zahlreiche Kooperationen mit internationalen Institutionen und Hochschulen in den Bereichen Ausbildung und Forschung ist ein großes Potenzial für Forschungsberichte vorhanden. In die Berichtreihe sollen sowohl hervorragende Diplom- und Projektarbeiten und Dissertationen als auch Forschungsberichte der Institutsmitarbeiter und Institutsgäste zu aktuellen Fragen der Techno- und Wirtschaftsmathematik aufgenommen werden.

Darüberhinaus bietet die Reihe ein Forum für die Berichterstattung über die zahlreichen Kooperationsprojekte des Instituts mit Partnern aus Industrie und Wirtschaft.

Berichterstattung heißt hier Dokumentation darüber, wie aktuelle Ergebnisse aus mathematischer Forschungs- und Entwicklungsarbeit in industrielle Anwendungen und Softwareprodukte transferiert werden, und wie umgekehrt Probleme der Praxis neue interessante mathematische Fragestellungen generieren.

Prof. Dr. Dieter Prätzel-Wolters
Institutsleiter

Kaiserslautern, im Juni 2001

Multi-reflection boundary conditions for lattice Boltzmann models

Irina Ginzburg
Fraunhofer Institut für Techno- und Wirtschaftsmathematik,
Gottlieb-Daimler-Strasse 49,
Kaiserslautern, D-67663, Germany
Email: ginzburg@itwm.fhg.de

and Dominique d'Humières
C.N.R.S. and Université Pierre et Marie Curie,
Laboratoire de Physique Statistique de l'E.N.S.,
24, rue Lhomond, 75231 Paris Cedex 05, FRANCE.
Email: dominiq@lps.ens.fr

submitted to *Physics of Fluids*

July 16, 2002

Abstract

We present a unified approach of several boundary conditions for lattice Boltzmann models. Its general framework is a generalization of previously introduced schemes such as the bounce-back rule, linear or quadratic interpolations, etc. The objectives are two fold: first to give theoretical tools to study the existing boundary conditions and their corresponding accuracy; secondly to design formally third-order accurate boundary conditions for general flows. Using these boundary conditions, Couette and Poiseuille flows are exact solution of the lattice Boltzmann models for a Reynolds number $Re = 0$ (Stokes limit).

Numerical comparisons are given for Stokes flows in periodic arrays of spheres and cylinders, linear periodic array of cylinders between moving plates and for Navier-Stokes flows in periodic arrays of cylinders for $Re < 200$. These results show a significant improvement of the overall accuracy when using the linear interpolations instead of the bounce-back reflection (up to an order of magnitude on the hydrodynamics fields). Further improvement is achieved with the new multi-reflection boundary conditions, reaching a level of accuracy close to the quasi-analytical reference solutions, even for rather modest grid resolutions and few points in the narrowest channels. More important, the pressure and velocity fields in the vicinity of the obstacles are much smoother with multi-reflection than with the other boundary conditions.

Finally the good stability of these schemes is highlighted by some simulations of moving obstacles: a cylinder between flat walls and a sphere in a cylinder.

1 Introduction

Boundary conditions in kinetic (or particle) methods, lattice Boltzmann model being one such example, are fundamentally different from their equivalent for more traditional Computational Fluid Dynamics (CFD) methods, such as finite-difference or finite-element ones. In many traditional CFD methods the boundary conditions (for instance fluid velocity, pressure, or some of their derivatives) are explicitly set on the nodes defining the mesh boundary. In kinetic methods, the particles (populations) leaving the computational domain have to be replaced by particles (populations) entering it. The properties of these entering particles define the boundary conditions and can be either given *a priori* or computed from those of the leaving particles. Such boundary conditions can only be set exactly from a perfect knowledge of the kinetic properties of the studied flow. In general this perfect knowledge is not available and some approximations have to be used, leading to some discrepancies between the particle distributions prescribed by the fluid dynamics and the boundary conditions. The resulting mismatch obviously limits the accuracy of modelling usual macroscopic boundary conditions by kinetic methods. It is well known in the context of rarefied gas dynamics that the physical effect of such mismatch creates a region, located near the boundary, where the discrepancy between the local distributions and the fluid

ones is exponentially damped away from it (see for instance [1]). This layer near the boundaries is known as Knudsen or accommodation layer and leads at the macroscopic level to an apparent non-zero velocity at the boundary (slip velocity). Moreover, in numerical methods using an underlying grid, the actual boundaries are not located on the grid points but at positions depending upon the details of the boundary conditions.

It has been recognized quite early that such effects indeed exist in lattice gases and lattice Boltzmann equation. In reference [2] Knudsen layers have been studied for two simple orientations of the boundary on a triangular lattice and it has been shown for Couette flows that the bounce-back condition locates the no-slip walls midway through the last fluid node and the first outside one. This result has been extended in [3, 4] to Poiseuille-Hagen flows for which it has been shown that exact parabolic profiles, for the same no-slip walls as in the Couette case, can be recovered for special relations between some eigenvalues of the collision operator. Despite these results there have been numerous attempts to still set the boundary conditions on the lattice nodes (see for instance [5, 6, 7, 8, 9], to name a few). Although most of them have given reasonable results for flat boundary parallel to the main lattice planes, they are not accurate enough when dealing with inclined flat walls or curved ones. To solve this problem we had proposed a different approach based on the reconstruction of the unknown populations from a second-order Chapman-Enskog expansion in [10]. Recently several authors have proposed various boundary conditions based on a link approach [11, 12, 13, 14, 15].

The motivation of the present work is to extend the results of [14] in order to derive formally third-order accurate boundary conditions for general flows, called here "multi-reflection". This study has been done in the context of moderate resolutions and/or moving boundaries. The analysis of the boundary conditions is done along the lines already introduced in [2, 3, 4]: the boundary condition is written as a closure relation between an unknown population entering the fluid and some others, known from the fluid dynamics; the populations are then replaced in the closure relation by their second-order approximations; finally a Taylor expansion of the result at the boundary node gives a second-order estimate of the perturbation of the ideal solution by boundary condition. If this estimate is zero, the boundary condition is formally third-order accurate. For some flows and geometries (for instance Poiseuille flows along the symmetry axis of the lattice), a non-zero estimate can be recast as a shift in the actual location of the walls and the boundary condition does not create Knudsen layers; this is not the case for

general flows and the estimate gives the order of magnitude of the Knudsen layer produced by the boundary condition.

The scope of this work is restricted to boundary conditions involving only populations moving along the same or opposite directions on the same line and on at most three fluid nodes at the same time. Presently the formal third-order accuracy of multi-reflection is proven theoretically and studied numerically for incompressible steady flows. The extension of these results to compressible and/or unsteady flows is left for future work.

In section 2 we give the general framework for our lattice Boltzmann models and sketch the associated Chapman-Enskog expansion. Section 3 is devoted to the definition of the boundary conditions considered here and to their theoretical analysis. The results are summarized in section 3.6. In section 4 the standard definition of the momentum exchange between the fluid and a boundary is recalled and a new definition is proposed to improve the accuracy. Using the $D3Q15$ model in three dimensions, these boundary conditions have been tested for Stokes flows over a cubic array of spheres in section 5.1.4, a square array of cylinders in section 5.1.5, and a periodic line of cylinders between moving walls in section 5.1.6. Results for Navier-Stokes flows over a square array of cylinders are given in section 5.2. In section 6 we presents some possible modifications of the static algorithms to deal with moving boundaries and we test them by simulating a cylinder moving between two parallel flat walls and a sphere moving in a cylinder.

2 Lattice Boltzmann models

2.1 General models

The lattice Boltzmann model considered here are defined on a cubic lattice in D dimensions by $b = b_m + 1$ velocities $\vec{c}_i$, $i \in \{0, \dots, b_m\}$ ($\vec{c}_0$ being a zero vector). The velocity set is chosen such that it has the same symmetry group as the cubic lattice; in particular it is invariant under the central symmetry (*i.e.* if $\vec{c}_q$ is an element of the set, $\vec{c}_{\bar{q}} = -\vec{c}_q$ is also an element), and the set is invariant by any exchange of coordinates.

These models obey the following evolution equation for the population f_i moving with velocity $\vec{c}_i$

$$f_i(\vec{r} + \vec{c}_i, t+1) = \tilde{f}_i(\vec{r}, t) \ , \tag{1}$$

$$\tilde{f}_i(\vec{r}, t) = f_i(\vec{r}, t) - (\mathsf{A} \cdot \mathbf{f}^{\text{ne.}}(\vec{r}, t))_i + t_p^\star \, \vec{c}_i \cdot \vec{F} \ , \tag{2}$$

where A is the collision matrix, the $t_p^\star$ are parameters given later (see eqs. (7) and (8), and table 1), $\vec{F}$ is a body force, and $\mathbf{f}^{\mathrm{ne.}} = \mathbf{f} - \mathbf{f}^{\mathrm{eq.}}$ ($\mathbf{f} = (f_i)$). The equilibrium distribution $\mathbf{f}^{\mathrm{eq.}} = (f_i^{\mathrm{eq.}})$ is a function of the conserved quantities ρ and $\vec{J}$ such that

$$\sum_{i=0}^{b_m} f_i^{\mathrm{eq.}} = \sum_{i=0}^{b_m} f_i = \rho \ , \tag{3}$$

$$\sum_{i=0}^{b_m} f_i^{\mathrm{eq.}} c_{i\alpha} = \sum_{i=0}^{b_m} f_i \, c_{i\alpha} = J_\alpha \ , \qquad \forall \alpha \ . \tag{4}$$

Here and in the sequel, greek subscripts stand for the spatial coordinates, x, y, and so on; in addition repeated greek indices correspond to implicit summations over the space coordinates.

The collision matrix A is defined by its eigenvectors $\mathbf{e}_k$ and eigenvalues λ_k (in the interval $]0, 2[$ for linear stability):

$$\mathsf{A} \cdot \mathbf{f}^{\mathrm{ne.}} = \sum_{k=0}^{b_m} \frac{\lambda_k}{\|\mathbf{e}_k\|^2} (\mathbf{f}^{\mathrm{ne.}} \cdot \mathbf{e}_k) \mathbf{e}_k \ . \tag{5}$$

As in [16], the eigenvectors $\mathbf{e}_k$ are built from polynomials of the components of the $\vec{c}_i$ which are then orthogonalized. The procedure starts with the $D+1$ b-vectors $\mathbf{e}_0$, $(\mathbf{e}_0)_i = 1$, and $\mathbf{e}_k$, $(\mathbf{e}_k)_i = c_{i\alpha}$ ($k \in \{1, \ldots, D\}$). It then proceeds with a b-vector $\mathbf{e}_{D+1}$ built on the $c_i^2 = \|\vec{c}_i\|^2$ and orthogonal to $\mathbf{e}_0$, $D-1$ pairwise orthogonal vectors built from $Dc_{i\alpha}^2 - c_i^2$, and $D(D-1)/2$ vectors $\mathbf{e}_k$, $(\mathbf{e}_k)_i = c_{i\alpha} c_{i\beta}$ with $\alpha \neq \beta$. Note that the preceding vectors have to be all non-zero in order to recover the usual Navier-Stokes equations. The procedure continues with higher degree polynomials and ends when the set of linearly independent orthogonal vectors has been exhausted. This construction is unique if it proceeds by increasing polynomial degrees and decreasing symmetry, *i. e.* b-vectors having in the physical space the symmetry of a scalar, then of a vector, a second rank tensor, and so on. This set of vectors $\mathbf{e}_k$ defines what is usually called the moment basis, the moments being the projections of population distribution $\mathbf{f}$ on them: $m_k = \mathbf{f} \cdot \mathbf{e}_k$. Finally the equilibrium is defined in the moment space as functions of the conserved quantities compatible with the symmetries of the lattice (see [15, 16, 17, 18, 19] for details and examples of moment bases).

2.2 Simplified models

Although the theory for boundary condition can be done in the above general framework, the algebra is simpler when using only two eigenvalues: λ_ν for the vectors $\mathbf{e}_k$ unchanged by central symmetry and λ_2 for the others, and the following equilibrium distribution

$$f_i^{\mathrm{eq.}}(\rho, \vec{J}) = t_p^\star \left(c_s^2 \rho + J_i\right) + 3t_p \frac{3j_i^2 - j^2}{2\tilde{\rho}} \,, \tag{6}$$

where $J_i = \vec{J}\cdot\vec{c}_i = J_\alpha c_{i\alpha}$, $j_i = \vec{j}\cdot\vec{c}_i = j_\alpha c_{i\alpha}$, $p = \|\vec{c}_i\|^2$, and $\tilde{\rho}$ is equal to $\rho(\vec{r},t)$ for the compressible Navier-Stokes equation and to ρ_0 for its incompressible variant (see [20, 21]). The t_p and $t_p^\star$ are model dependent and must obey at least the constraints

$$\sum_{i=0}^{b_m} t_p = \sum_{i=0}^{b_m} t_p^\star c_s^2 \;=\; 1 \,, \tag{7}$$

$$3\sum_{i=0}^{b_m} t_p c_{i\alpha} c_{i\beta} = \sum_{i=0}^{b_m} t_p^\star c_{i\alpha} c_{i\beta} \;=\; \delta_{\alpha\beta} \,, \qquad \forall \alpha, \beta \,, \tag{8}$$

coming from the conservation laws (3) and (4). The momentum $\vec{j}$ used in the nonlinear term of equation (6) is defined as

$$\vec{j} = \vec{J} - I_{\mathrm{f}}\vec{F} \,, \tag{9}$$

where $I_{\mathrm{f}} = 0$ for the standard definition and $I_{\mathrm{f}} = -1/2$ for the modified one which is used here (see [3, 22, 23, 24]). The "incompressible" variant with $\tilde{\rho} = \rho_0$ has also been used for all the steady simulations presented here.

Model	t_0	$t_0^\star$	$t_1^\star = 3t_1$	$t_2^\star = 3t_2$	$t_3^\star = 3t_3$
$D2Q9$	$\frac{4}{9}$	$\frac{3-5c_s^2}{3c_s^2}$	$\frac{1}{3}$	$\frac{1}{12}$	–
$D3Q15$	$\frac{2}{9}$	$\frac{3-7c_s^2}{3c_s^2}$	$\frac{1}{3}$	–	$\frac{1}{24}$

Table 1: Equilibrium weights t_p and $t_p^\star$.

The parameters t_p and $t_p^\star$ are given for the $D2Q9$ and $D3Q15$ models in table 1 (note that the t_p are those given in [25, 26] and the $t_p^\star$ are defined to keep the speed of sound as a free parameter). With these choices the nonlinear terms and the viscosity are isotropic and the viscosity is given by

$$\nu = \frac{1}{3}\left(\frac{1}{\lambda_\nu} - \frac{1}{2}\right) = \frac{2\tau - 1}{6} \ , \tag{10}$$

with $\tau = 1/\lambda_\nu$.

In the simulations reported in section 5.1, we use the following equilibrium

$$f_i^{\text{eq.}}(\rho, \vec{J}) = t_p^\star \left(c_s^2 \rho + J_i\right) , \tag{11}$$

which leads to the Stokes equation which is written for stationary incompressible case as

$$\nabla P - \vec{F} = \nu \Delta \vec{j} \, , \quad \nabla \cdot \vec{j} = 0 \ , \quad P = c_s^2 \rho \ . \tag{12}$$

2.3 Simplified Chapman-Enskog expansion

Neglecting the third-order and higher derivatives of the momentum and the second-order and higher derivatives of the density and of the non-linear terms, the populations can be approximated as

$$f_i \approx f_i^{\text{eq.}} + f_i^{(1)} + f_i^{(2)} \ , \tag{13}$$

where $f_i^{(1)}$ is related to the first-order derivatives of the momentum through some second-order tensor $E_{i\alpha\beta}^{(2)}$ by

$$f_i^{(1)} = -\frac{1}{\lambda_\nu} \partial_\beta j_\alpha E_{i\alpha\beta}^{(2)} \ , \tag{14}$$

and $f_i^{(2)}$ is related to the second-order derivatives of the momentum and the first-order derivatives of the non-linear terms through some third-order tensor $E_{i\alpha\beta\gamma}^{(3)}$ by

$$f_i^{(2)} = \frac{1}{\lambda_2}\left(\nu \partial_{\beta\gamma} j_\alpha - \partial_\gamma \frac{j_\alpha j_\beta}{2\tilde{\rho}}\right) E_{i\alpha\beta\gamma}^{(3)} \ . \tag{15}$$

The projections of the tensors $E_{i\alpha\beta}^{(2)}$ and $E_{i\alpha\beta\gamma}^{(3)}$ on the first $D+1$ vectors $\mathbf{e}_k$ must be equal to zero due to the conservation laws (3) and (4). Since $\partial_{\beta\gamma} j_\alpha$

is unchanged by a central symmetry while $\partial_{\beta\gamma} j_\alpha$ and $\partial_\gamma (j_\alpha j_\beta/(2\tilde{\rho}))$ change their signs, it comes

$$(\mathsf{A} \cdot \mathbf{f}^{\text{ne.}})_i = \lambda_\nu f_i^{(1)} + \lambda_2 f_i^{(2)} \ . \tag{16}$$

Taking the value of the terms in equation (13) at $(\vec{r}, t)$ and $(\vec{r} + \vec{c}_i, t+1)$, the Taylor expansion of the difference $f_i(\vec{r} + \vec{c}_i, t+1) - f_i(\vec{r}, t)$ must be equal to the corresponding expansion of $-(\mathsf{A} \cdot \mathbf{f}^{\text{ne.}})_i + t_p^\star \vec{c}_i \cdot \vec{F}$. After some tedious but straightforward algebra, one gets

$$E^{(2)}_{i\alpha\beta} = t_p^\star (c_{i\alpha} c_{i\beta} - c_s^2 \delta_{\alpha\beta}) \ , \tag{17}$$

and

$$E^{(3)}_{i\alpha\beta\gamma} = t_p^\star (3 c_{i\alpha} c_{i\beta} c_{i\gamma} - c_{i\alpha}\delta_{\beta\gamma} - c_{i\beta}\delta_{\alpha\gamma} - c_{i\gamma}\delta_{\alpha\beta}) \ . \tag{18}$$

The tensors $E^{(2)}_{i\alpha\beta}$ and $E^{(3)}_{i\alpha\beta\gamma}$ are unchanged by any permutation of their Greek subscripts. In general their components are linear combinations of the components of the $\mathbf{e}_k$'s introduced in section 2.1. For the $D2Q9$ and $D3Q15$ models considered here, most of the components $E^{(2)}_{i\alpha\beta}$ and $E^{(3)}_{i\alpha\beta\gamma}$ are equal to components of some $\mathbf{e}_k$, except for the $E^{(2)}_{i\alpha\alpha}$. Writing

$$E^{(2)}_{i\alpha\alpha} = t_p^\star \left(\left(c_{i\alpha}^2 - \frac{c_i^2}{D} \right) + \left(\frac{c_i^2}{D} - c_s^2 \right) \right) \ , \tag{19}$$

the $E^{(2)}_{i\alpha\alpha}$ are linear combinations of the moments built on $D c_{i\alpha} c_{i\alpha} - c_i^2$ and of $c_i^2 - D c_s^2$. The latter components can be expressed in turn as linear combinations, depending on c_s^2, of the $\mathbf{e}_k$'s built on c_i^2 and c_i^4.

For the models such that $c_{i\alpha}^3 = c_{i\alpha}$, the diagonal elements of $E^{(3)}_{i\alpha\beta\gamma}$ are zero: $E^{(3)}_{i\alpha\alpha\alpha} = 0$. For the $D2Q9$ model, $E^{(3)}_{ixyy}$ and $E^{(3)}_{iyxx}$ are, up to a multiplicative constant, the components of the two "cubic" $\mathbf{e}_k$'s. For the $D3Q15$ model, $E^{(3)}_{ixyy} = E^{(3)}_{ixzz}$ and $E^{(3)}_{ixyz} \neq 0$; with their independent permutations of x, y, and z, they are, up to a multiplicative constant, the components of the four cubic $\mathbf{e}_k$'s.

3 Six-population boundary conditions

3.1 Definitions

The boundary conditions presented here are based on the following definitions:

1. **Fluid nodes** are defined as the nodes $\vec{r}$ such that

   a) the collision step is given by eq. (2) without any change;

   b) the propagation step between them is given by eq. (1).

   The set of fluid nodes is denoted $\mathcal{F}$. The nodes which are not in $\mathcal{F}$ are considered as "outside" nodes.

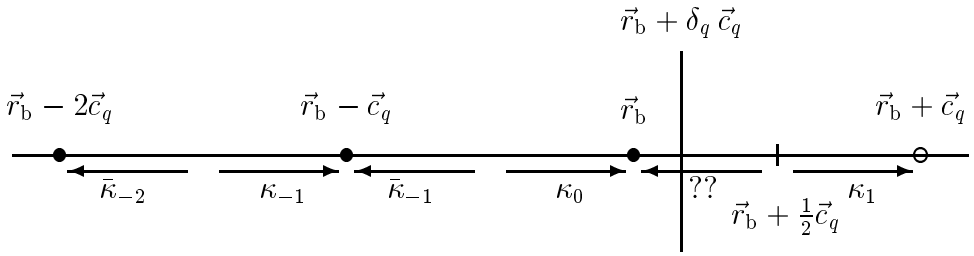

Figure 1: A boundary surface cutting at $\vec{r}_\mathrm{b} + \delta_q\,\vec{c}_q$ the link between fluid node $\vec{r}_\mathrm{b}$ and an outside one at $\vec{r}_\mathrm{b} + \vec{c}_q$. The solid circles represent the fluid nodes and the open circle represents an "outside" node.

2. A **boundary node** $\vec{r}_\mathrm{b} \in \mathcal{B}$ is defined as a fluid node having at least one neighbor $\vec{r}_\mathrm{b} + \vec{c}_q$ (where $\vec{c}_q \in \{\vec{c}_i\}$) which is not a fluid node. The set of boundary nodes and the set of cut links (connecting a boundary node to an outside one) are denoted $\mathcal{B}$ and $\mathcal{C}$ respectively.

3. The boundary conditions are given on a $(D-1)$-surface Ω which intersects the link between $\vec{r}_\mathrm{b}$ and $\vec{r}_\mathrm{b} + \vec{c}_q$ at $\vec{r}_\mathrm{b} + \delta_q\,\vec{c}_q$ (see Fig. 1). We here consider only Dirichlet boundary conditions corresponding to a given velocity $\vec{u}_\mathrm{w}(\vec{r}_\mathrm{b} + \delta_q\vec{c}_q, t+1)$ on Ω. The associated momentum $\vec{j}_w$ is defined by

$$\vec{j}_w = \tilde{\rho}_\mathrm{b}\vec{u}_\mathrm{w}\ , \tag{20}$$

   where $\tilde{\rho}_\mathrm{b}$ is equal to $\rho(\vec{r}_\mathrm{b}, t)$ for the compressible Navier-Stokes and to ρ_0 for its incompressible variant [20, 21], according to the choice made for equation (6) .

After the propagation step at t, the post-collision population $\tilde{f}_q(\vec{r}_\mathrm{b}, t)$ has left the fluid and can be thought to be on the outside node $\vec{r}_\mathrm{b} + \vec{c}_q$ as

$f_q(\vec{r}_{\rm b}+\vec{c}_q,t+1)$. At the same time the population $f_{\bar{q}}(\vec{r}_{\rm b},t+1)$, corresponding to the direction $\vec{c}_{\bar{q}}=-\vec{c}_q$, is unknown and has to be supplied by the boundary condition. In the sequel we will restrict our attention to the following closure relation

$$\begin{aligned} f_{\bar{q}}(\vec{r}_{\rm b},t+1) &= \kappa_1 f_q(\vec{r}_{\rm b}+\vec{c}_q,t+1) \\ &+ \kappa_0 f_q(\vec{r}_{\rm b},t+1)+\kappa_{-1} f_q(\vec{r}_{\rm b}-\vec{c}_q,t+1) \\ &+ \bar{\kappa}_{-1} f_{\bar{q}}(\vec{r}_{\rm b}-\vec{c}_q,t+1)+\bar{\kappa}_{-2} f_{\bar{q}}(\vec{r}_{\rm b}-2\vec{c}_q,t+1) \\ &- w_q t_p^\star j_{q\rm w}+t_p^\star F_{\bar{q}}^{\rm p.c.} \ , \end{aligned} \tag{21}$$

where the symbols with an overbar refer to quantities associated with $\vec{c}_{\bar{q}}$. The coefficients κ_1, κ_0, $\bar{\kappa}_{-1}$, κ_{-1}, $\bar{\kappa}_{-2}$ are referred to as the coefficients of the interpolations or of the multi-reflection boundary condition. The term $w_q t_p^\star j_{q\rm w}$ is used to set the Dirichlet boundary condition ($j_{q\rm w}=\vec{\jmath}_w\cdot\vec{c}_q$). The term $F_{\bar{q}}^{\rm p.c.}$ is discussed in section 3.5.

Using (1), the relation (21) can also be written in term of the post-collision distributions, either for some terms or for all of them as in

$$\begin{aligned} f_{\bar{q}}(\vec{r}_{\rm b},t+1) &= \kappa_1 \tilde{f}_q(\vec{r}_{\rm b},t) \\ &+ \kappa_0 \tilde{f}_q(\vec{r}_{\rm b}-\vec{c}_q,t)+\kappa_{-1} \tilde{f}_q(\vec{r}_{\rm b}-2\vec{c}_q,t) \\ &+ \bar{\kappa}_{-1} \tilde{f}_{\bar{q}}(\vec{r}_{\rm b},t)+\bar{\kappa}_{-2} \tilde{f}_{\bar{q}}(\vec{r}_{\rm b}-\vec{c}_q,t) \ , \\ &- w_q t_p^\star j_{q\rm w}+t_p^\star F_{\bar{q}}^{\rm p.c.} \ . \end{aligned} \tag{22}$$

The choice between (21) and (22) is mostly a matter of taste. The equations (28) and (30) below have been obtained with (22); using (21) instead leads to the same final results for steady Stokes flows, but with different intermediate steps.

The above boundary condition has the following properties. First, with $F_{\bar{q}}^{\rm p.c.}=0$, it is a generalization of the bounce-back rule (with the Dirichlet condition) and of the linear and quadratic interpolations introduced in [14]: bounce-back corresponds to

$$\kappa_1=1 \ , \quad w_q=2 \ , \quad \text{and} \quad \kappa_0=\kappa_{-1}=\bar{\kappa}_{-1}=\bar{\kappa}_{-2}=0 \ , \tag{23}$$

the upwind linear interpolation for $0\le\delta_q\le 1/2$ corresponds to

$$\kappa_1=2\delta_q \ , \quad \kappa_0=1-2\delta_q \ , \quad w_q=2 \ , \quad \text{and} \quad \kappa_{-1}=\bar{\kappa}_{-1}=\bar{\kappa}_{-2}=0 \ , \tag{24}$$

and the downwind linear interpolation for $1/2 \leq \delta_q$ corresponds to

$$\kappa_1 = \frac{1}{2\delta_q} , \quad \bar{\kappa}_{-1} = \frac{2\delta_q - 1}{2\delta_q} , \quad w_q = \frac{1}{\delta_q} ,$$
$$\text{and} \quad \kappa_0 = \kappa_{-1} = \bar{\kappa}_{-2} = 0 . \tag{25}$$

The upwind (respectively downwind) quadratic interpolations in [14] correspond to $\bar{\kappa}_{-1} = \bar{\kappa}_{-2} = 0$ (respectively $\kappa_0 = \kappa_{-1} = 0$), the other coefficients being given in their equation (6a) (respectively (6b), their q being replaced by our δ_q).

Secondly the relations (21) and (22) involve only the populations considered in [14].

Finally all the required information is available at the boundary node $\vec{r}_{\rm b}$ and its fluid neighbor $\vec{r}_{\rm b} - \vec{c}_q$, using their four post-collision distributions at time t, see (22), and $f_q(\vec{r}_{\rm b} - \vec{c}_q, t+1)$ after the propagation step. This property is quite important for parallel codes in which the communications are restricted to the nearest neighbors along $\pm\vec{c}_q$. Equation (22) requires three fluid nodes along the link in order to be used as such. When there are only two fluid nodes available, the equation can be modified in several ways. The simplest one, used here, consists in replacing $f_q(\vec{r}_{\rm b} - \vec{c}_q, t+1)$ by $f_q(\vec{r}_{\rm b} - \vec{c}_q, t)$ in relation (21). A second one applies when the boundary for $\vec{r}_{\rm b} - 2\vec{c}_q$ is a flat wall located at $\delta_q = 1/2$; in this case the bounce-back condition is applied first and its result provides the missing population.

3.2 Closure relation

In the sequel we use the following notations: $j_q = \vec{j} \cdot \vec{c}_q$ and $F_q = \vec{F} \cdot \vec{c}_q$ are the projections of $\vec{j}$ and $\vec{F}$ on $\vec{c}_q$; ∂_q and ∂_{qq} are the first and second derivatives along $\vec{c}_q$ ($\partial_q = c_{q\alpha}\partial_\alpha$). With these notations the first and second order non-equilibrium terms (26) and (27) become respectively

$$f_q^{(1)} = -t_p^\star \frac{1}{\lambda_\nu} (\partial_q j_q - c_s^2 \nabla \cdot \vec{j}) . \tag{26}$$

and

$$f_q^{(2)} = t_p^\star \frac{1}{\lambda_2} \left(\nu \left(3\partial_{qq} j_q - \Delta j_q - 2\partial_q \nabla \cdot \vec{j} \right) - \partial_q \frac{3j_q^2 - j^2}{2\tilde{\rho}} + \partial_\alpha \frac{j_\alpha j_q}{\tilde{\rho}} \right) . \tag{27}$$

The closure relation (21) is then analyzed by replacing the distributions f_q and $f_{\bar{q}}$ (or $\tilde{f}_q$ and $\tilde{f}_{\bar{q}}$) by their second order Chapman-Enskog expansion. This first step is followed by a Taylor expansion of the conserved quantities around their values at $\vec{r}_{\rm b}$ (see appendix A). For incompressible flows $\nabla\cdot\vec{j}=0$, relation (21) leads to

$$\begin{aligned} & A_0 j_q + A_1 \partial_q j_q + A_2 \partial_{qq} j_q + F_{\bar{q}}^{\rm p.c.} + (A_{\rm P}-1)\left(P + \frac{3j_q^2 - j^2}{2\tilde{\rho}}\right) \\ + \;& A_\nu \left(\nu \Delta j_q + \partial_q \frac{3j_q^2 - j^2}{2\tilde{\rho}} - \partial_\alpha \frac{j_\alpha j_q}{\tilde{\rho}}\right) + A'_{\rm P} \partial_q \left(P + \frac{3j_q^2 - j^2}{2\tilde{\rho}}\right) \\ + \;& A_{\rm F} F_q = w_q j_{q{\rm w}} + O(\nabla\cdot\vec{j}) + O(\epsilon^3), \end{aligned} \tag{28}$$

with

$$\begin{aligned} A_{\rm P} &= \kappa_1 + \kappa_0 + \bar{\kappa}_{-1} + \kappa_{-1} + \bar{\kappa}_{-2} = 1 \ , \\ A_0 &= 2 - 2(\bar{\kappa}_{-1} + \bar{\kappa}_{-2}) \ , \\ A_1 &= 1 - (\kappa_0 + 2\kappa_{-1} - \bar{\kappa}_{-2}) \ , \\ A_{\rm F} &= 1 - 2(\bar{\kappa}_{-1} + \bar{\kappa}_{-2}) + 2I_{\rm f}(1 - (\bar{\kappa}_{-1} + \bar{\kappa}_{-2})) \ , \\ A'_{\rm P} &= -(\kappa_0 + 2\kappa_{-1} + \bar{\kappa}_{-2}) \ , \\ A_2 &= -3\nu A_\nu + A_j + A_{j'} \ , \\ A_\nu &= -\left[\frac{1}{\lambda_2} + \left(\frac{1}{\lambda_2} - 1\right)(1 - 2(\bar{\kappa}_{-1} + \bar{\kappa}_{-2}))\right] , \\ A_j &= \left(\frac{\kappa_0}{2} + 2\kappa_{-1} - \frac{\bar{\kappa}_{-2}}{2}\right) \ , \\ A_{j'} &= \left(\frac{1}{\lambda_\nu} - 1\right)(\kappa_0 + 2\kappa_{-1} + \bar{\kappa}_{-2}) \ , \end{aligned} \tag{29, 30}$$

where the term κ_1 has been removed from A_0 to $A_{j'}$ using $A_{\rm P}=1$. Note that the non-linear terms disappear when the linear equilibrium (11) is used; then (28) is obviously verified for the linear equilibrium if the flow and the forcing are perpendicular to $\vec{c}_q$ ($j_q = j_{q{\rm w}} = F_q = 0$), $\partial_q P = 0$, and $F_{\bar{q}}^{\rm p.c.} = 0$.

3.3 Couette flow

Let us first consider the flow between two parallel planes moving with parallel but different velocities. The corresponding steady flow, called Couette flow, is a pure shear flow for which the density is uniform and only the first-order

spatial derivatives are non-zero (uniform shear). Taking $F_{\bar{q}}^{\mathrm{p.c.}} = 0$ and the **linear** equilibrium (11), eq. (28) becomes

$$A_0 j_q + A_1 \partial_q j_q = w_q j_{q\mathrm{w}} \ . \tag{31}$$

Then the Dirichlet boundary condition $j_{q\mathrm{w}}$ is met at $\vec{r}_{\mathrm{b}} + \delta_q \vec{c}_q$ when the following conditions are satisfied

$$\frac{A_1}{A_0} = \delta_q \ , \tag{32}$$

$$w_q = A_0 \ . \tag{33}$$

Using eqs. (29), (32), and (33) the coefficients κ_1, κ_0, and w_q must be related to the other ones by

$$\kappa_1 = 2\delta_q + \kappa_{-1} - (1+2\delta_q)\bar{\kappa}_{-1} - (2+2\delta_q)\bar{\kappa}_{-2} \ , \tag{34}$$

$$\kappa_0 = 1 - 2\delta_q - 2\kappa_{-1} + 2\delta_q\bar{\kappa}_{-1} + (1+2\delta_q)\bar{\kappa}_{-2} \ , \tag{35}$$

$$w_q = 2(1 - \bar{\kappa}_{-1} - \bar{\kappa}_{-2}) \ . \tag{36}$$

For the bounce-back coefficients (23) these conditions are satisfied only if $\delta_q = 1/2$. This is possible only when the moving planes are parallel to the symmetry planes of the underlying lattice, for which the links are either perpendicular to the velocity or cut midway through the boundary nodes and the nearest outside ones. For these special orientations of the moving planes, the solution of the linear LB equation with bounce-back is exact (up to machine accuracy) if the planes are located at $\delta_q = 1/2$ (as found in [2]); note that this exact solution is lost and the apparent convergence rate is only first-order in the grid resolution if the planes are mistakenly located on the boundary nodes or on the nearest outside ones. For the other orientations of the moving planes, the bounce-back rule is no longer compatible with Couette flows. Since for these orientations δ_q takes values between 0 and 1, one expects a first-order convergence rate with the grid resolution.

When the multi-reflection coefficients are chosen such that the relations (34) to (36) hold for all the boundary nodes and links, the Couette flow is an exact solution of the linear LB equation with the corresponding boundary conditions for any orientation of the moving planes and any distances between them. It is easy to check that this is the case for the linear interpolations (24) and (25).

At this point it important to realize that the relations (34) to (36) are necessary conditions for any order (≥ 1) boundary conditions and apply implicitly in the following sections.

3.4 Poiseuille-Hagen flow between parallel plates

Let us now consider the flow between two parallel plane walls, at rest and symmetric with respect to the origin, and due to uniform forcing $\vec{F}$ parallel to the walls. Along any line parallel to $\vec{c}_q$ the coordinates x_q are defined using $\vec{c}_q$ as unit vector and the center of the fluid segment as origin. Then the planes intersect the line at $\pm(x_{q\mathrm{b}} + \delta_q)$ and the exact solution of the **linear** LB equation is a parabolic flow given by

$$j_q = j_{0q}\left(1 - \frac{4x_q^2}{H_{\mathrm{eff}}^2}\right) , \tag{37}$$

where H_{eff} is an effective length depending on the boundary condition. Denoting Θ the projection of $\vec{c}_q$ on the direction perpendicular to the walls (in lattice unit), j_{0q} is related to $\vec{F}$, H_{eff}, and ν by

$$F_q = j_{0q}\frac{8\nu\Theta^2}{H_{\mathrm{eff}}^2} , \tag{38}$$

since $\partial_q P = 0$ and $\partial_{qq} j_q = \Theta^2 \Delta j_q$ for Poiseuille flows. Using (37) and neglecting the non-linear terms (linear equilibrium (11)), equation (28) leads to the following relation between H_{eff} and the prescribed one $H_q = 2(x_{q\mathrm{b}} + \delta_q)$ along $\vec{c}_q$:

$$\begin{aligned} H_{\mathrm{eff}}^2 &= H_q^2 + 6\Lambda^2 - 4\delta_q^2 - \frac{8\nu}{\Theta^2}\left(\frac{1}{\lambda_2} + I_{\mathrm{f}}\right) + \frac{4(\kappa_{-1} - \bar{\kappa}_{-2})}{1 - \bar{\kappa}_{-1} - \bar{\kappa}_{-2}} \\ &+ \frac{12\nu}{1 - \bar{\kappa}_{-1} - \bar{\kappa}_{-2}}(1 - 2\delta_q + (1 + 2\delta_q)\bar{\kappa}_{-1} + (3 + 2\delta_q)\bar{\kappa}_{-2}) , \end{aligned} \tag{39}$$

where

$$\Lambda^2 = \frac{4}{3}\left(\frac{1}{\lambda_\nu} - \frac{1}{2}\right)\left(\frac{1}{\lambda_2} - \frac{1}{2}\right) . \tag{40}$$

For a forcing along one of the main axes (x, y, etc.), $\Theta^2 = 1$ and (40) relates the effective width of the parabolic profile to its prescribed value.

For the bounce-back rule ($\delta_q = 1/2$) and $\Theta^2 = 1$, taking $I_{\mathrm{f}} = -1/2$ eq. (39) becomes

$$D_{\mathrm{eff}}^2 = D_{1/2}^2 + 4\Lambda^2 - 1 , \tag{41}$$

where D_{eff} is the effective diameter and $D_{1/2}$ is the diameter based on the middle of the cut links. For $\Lambda^2 = 1/4$ or

$$\lambda_2(\lambda_\nu) = 8\frac{2-\lambda_\nu}{8-\lambda_\nu}\,. \tag{42}$$

the Poiseuille profile is the exact Poiseuille solution found in [3, 4] for walls located at $\pm(x_{q\text{b}} + 1/2)$, as for Couette flows. Note that for BGK models ($\lambda_2 = \lambda_\nu$), $\Lambda^2 = 12\nu$ and the walls are located exactly at $\pm(x_{q\text{b}} + 1/2)$ for $\nu = 1/\sqrt{48}$. When $\Lambda^2 \neq 1/4$, the relative error made by taking $H_{1/2}$ instead of H_{eff} is approximatively $(4\Lambda^2 - 1)/(2H_{1/2}^2)$. Then locating the walls on the middle of the cut links is second-order accurate, however the prefactor $4\Lambda^2 - 1$ can be large for large values of Λ^2. For the BGK case, the prefactor is $48\nu^2 - 1$ and increases very rapidly with the viscosity: for instance if $H_{1/2} = 10$ lattice units and $\nu = 1$ ($\tau = 7/2$), $H_{\text{eff}} \approx 12.1$, *i. e.* the relative error is larger than 20% (for $\tau = 50$, the effective width is larger than 11 times the prescribed one, see for instance Fig. 2 in reference [7]).

A very important property of the bounce-back condition for the measurements reported in section 5.1 is that the permeability is independent of the viscosity if the coefficient Λ^2 is kept constant, even for arbitrary complex flows. For each particular flow, the precision can be further improved for an appropriate choice of the free parameter Λ^2 [27] (a good starting value being in general close to 1/4). So far we have been unable to prove theoretically this property, however this is strongly confirmed by all our numerical simulations (see section 5.1.3).

For the interpolations of [14] and $\Theta^2 = 1$, equation (41) gives the error in the wall location as a function of ν and Λ^2. It is again possible to choose λ_2 as a function of λ_ν to set this error to zero, but this is no longer possible for a fixed value of Λ^2. For arbitrary inclined Poiseuille flows, the errors cannot be canceled for all the values of δ_q for constant values of λ_ν, λ_2, and I_{f}. As a consequence, none of the interpolations of [14] give exact parabolic profiles for arbitrary inclined Poiseuille flows.

By setting two coefficients in the set $\{\kappa_0, \kappa_{-1}, \bar{\kappa}_{-1}, \bar{\kappa}_{-2}\}$ to zero, we have been able to derive six sets of relations, for the three other coefficients, giving exact inclined Poiseuille flows. In addition these sets are independent of Θ for $I_{\text{f}} = -1/\lambda_2$. However we did not succeeded to find rules to choose among them as a function of δ_q in order to guarantee numerical stability. In addition, we think these results are superseded by the results of the next section.

3.5 General flows

The Dirichlet boundary condition, exact up to second-order:

$$j_{q\mathrm{w}}(\vec{r}_{\mathrm{b}}+\delta_q\,\vec{c}_q)=j_q(\vec{r}_{\mathrm{b}}+\delta_q\,\vec{c}_q)=(j_q+\delta_q\partial_q j_q+\frac{1}{2}{\delta_q}^2\partial_{qq}j_q)(\vec{r}_{\mathrm{b}})\ , \tag{43}$$

is obtained from (28), when the following relations are verified (sufficient conditions)

$$\begin{aligned} I_{\mathrm{f}}=-\frac{1}{2}\ ,\ A_{\mathrm{F}} &= 0\ ,\ A'_{\mathrm{P}}=0\ ,\\ \frac{A_1}{A_0} &= \delta_q\ ,\ \frac{A_2+G^{\mathrm{p.c.}}}{A_0}=\frac{1}{2}{\delta_q}^2\ , \end{aligned} \tag{44}$$

where $G^{\mathrm{p.c.}}$ is defined by

$$G^{\mathrm{p.c.}}\partial_{qq}j_q=A_\nu\Delta j_q+F_{\bar{q}}^{\mathrm{p.c.}}\ . \tag{45}$$

The conditions $I_{\mathrm{f}}=-1/2$ and $A_{\mathrm{F}}=0$ implies $A_0=2$, $\bar{\kappa}_{-1}=-\bar{\kappa}_{-2}$, and $A_\nu=-\Lambda^2/2$. Since the relation between Δj_q and $\partial_{qq}j_q$ is not known *a priori* for general flows, the condition (45) cannot be satisfied if $F_{\bar{q}}^{\mathrm{p.c.}}=0$. Noticing that Δj_q and the non-linear terms appear in eq. (27), they can be removed from eq. (28) by setting

$$t_p^\star F_{\bar{q}}^{\mathrm{p.c.}} = \frac{\Lambda^2}{2\nu}\tilde{f}_q^{(2)}=-\frac{\Lambda^2}{2\nu}\lambda_2 f_q^{(2)}\ . \tag{46}$$

From a technical point of view, $\tilde{f}_q^{(2)}$ is computed from the part of the sum in (5) restricted to the $\mathbf{e}_k$ built from the third order polynomials (the non-zero $E^{(3)}_{i\alpha\beta\gamma}$ in section 2.3).

With the above definition of $F_{\bar{q}}^{\mathrm{p.c.}}$, $G^{\mathrm{p.c.}}=-3\Lambda^2/2$ and (44) leads to

$$\begin{aligned} \kappa_1 &= 2\delta_q+\delta_q^2\ ,\\ \kappa_0 &= \frac{3}{2}-3\delta_q-2\delta_q^2\ ,\\ \kappa_{-1} &= -\frac{1}{2}+\delta_q+\delta_q^2\ ,\\ \bar{\kappa}_{-1} &= \frac{1}{2}-\delta_q\ ,\\ \bar{\kappa}_{-2} &= -\frac{1}{2}+\delta_q\ ,\\ w_q &= 2\ . \end{aligned} \tag{47}$$

It is easy to check that $0 \leq \kappa_1 \leq 3$, $-7/2 \leq \kappa_0 \leq 3/2$, and $-1/2 \leq \kappa_{-1} \leq 3/2$ for $0 \leq \delta_q \leq 1$, *i. e.* these coefficients have values outside the interval $[-1,1]$ for some value of δ_q. Although we do not have solid stability analysis for the boundary conditions, we have found numerically that values outside $[-1,1]$ very often lead to numerical instabilities.

Noticing that the macroscopic closure relation (28) is not changed, at least up to third order, under the following transformation:

$$\begin{aligned}
&\kappa_1 \;\to\; (\kappa_1-\kappa)/(\kappa+1)\;, && \kappa_0 \;\to (\kappa_0+2\kappa)/(\kappa+1)\\
&\kappa_{-1} \to (\kappa_{-1}-\kappa)/(\kappa+1)\;, && \bar{\kappa}_{-1} \to (\bar{\kappa}_{-1}+2\kappa)/(\kappa+1)\;,\\
&\bar{\kappa}_{-2} \to (\bar{\kappa}_{-2}-\kappa)/(\kappa+1)\;, && w_q \;\to w_q/(\kappa+1)\;,\\
& && F_{\vec{q}}^{\mathrm{p.c.}} \to F_{\vec{q}}^{\mathrm{p.c.}}/(\kappa+1)\;,
\end{aligned} \tag{48}$$

where κ is an arbitrary constant, a one parameter family of coefficient can be constructed. In order to show this result, one has to use the projected stationary Navier-Stokes equation:

$$\partial_\alpha \frac{j_\alpha j_q}{\tilde{\rho}} + \partial_q P = F_q + \nu \Delta j_q\;. \tag{49}$$

For instance taking

$$\kappa = -\frac{1}{2}(1-2\delta_q-\delta_q^2)\;, \tag{50}$$

leads to a new set of coefficients

$$\begin{aligned}
\kappa_1 &= 1\\
\kappa_0 &= -\bar{\kappa}_{-1} = \frac{1-2\delta_q-2\delta_q^2}{(1+\delta_q)^2}\\
\kappa_{-1} &= -\bar{\kappa}_{-2} = \frac{\delta_q^2}{(1+\delta_q)^2}\;,\\
w_q &= \frac{4}{(1+\delta_q)^2}\;,
\end{aligned} \tag{51}$$

which stay in the interval $[-1,1]$ for $0 \leq \delta_q \leq 1$. This set of coefficients share some properties of the bounce-back condition. On the positive side the higher order errors (hence the permeability) are found independent of the viscosity for fixed values of Λ^2. On the negative side the corresponding

boundary condition for the staggered invariants is a free-slip condition, *i. e.* the staggered invariants are not damped by the boundary when they appear. As for bounce-back, this effect can be killed by using $f_q(\vec{r}_{\rm b}+\vec{c}_q,t)$ instead of $f_q(\vec{r}_{\rm b}+\vec{c}_q,t+1)$ in (21) [28].

A probably better way to avoid staggered invariants is to derive an other set of coefficients with $\kappa_1 \neq 1$ for $\delta_q > 0$ and the following constraints:

$$0 \leq \kappa_1 \leq 1 \text{ and } \{\kappa_0, \kappa_{-1}, \bar{\kappa}_{-1}, \bar{\kappa}_{-2}\} \in [-1,1] \ , \quad \text{for } 0 \leq \delta_q \leq 1 \ . \tag{52}$$

Introducing the following polynomials of δ_q:

$$\begin{aligned} \kappa_{\rm t} &= 3 + 2\delta_q \ , \\ \kappa_{\rm s} &= 1 + 6\delta_q + 4\delta_q^2 \ , \\ \kappa_{\rm f} &= (\kappa_{\rm t} + \kappa_{\rm s})/2 = 2(1+\delta_q)^2 \ , \end{aligned} \tag{53}$$

the family of coefficients derived from (47) with the transformation (48) can be written as

$$\begin{aligned} \kappa_1 &= \frac{\kappa^* \kappa_{\rm f}}{\kappa_{\rm s}} - 1 \ , \\ \kappa_0 &= 2 - \kappa^* \ , \\ \kappa_{-1} &= (\kappa_{\rm f} - \kappa_{\rm t} + 2)\frac{\kappa^*}{\kappa_{\rm s}} - 1 \ , \\ \bar{\kappa}_{-1} &= 2 - \frac{\kappa^* \kappa_{\rm t}}{\kappa_{\rm s}} \ , \\ \bar{\kappa}_{-2} &= (\kappa_{\rm t} - 2)\frac{\kappa^*}{\kappa_{\rm s}} - 1 \ , \\ w_q &= \frac{4\kappa^*}{\kappa_{\rm s}} \ , \end{aligned} \tag{54}$$

where the parameter κ^* has been chosen such that $\kappa_0 = 2 - \kappa^*$. The constraints (52) are satisfied provided that

$$\max\{1, \frac{\kappa_{\rm s}}{\kappa_{\rm t}}\} \leq \kappa^* \leq \frac{2\kappa_{\rm s}}{\kappa_{\rm f}} \ . \tag{55}$$

The upper bound corresponds to the solution (51). The lower bound is 1 for $0 \leq \delta_q \leq \delta_0$ ($\kappa_0 = 1$) and $\kappa_{\rm s}/\kappa_{\rm t}$ for $\delta_0 \leq \delta_q \leq 1$ ($\bar{\kappa}_{-1} = 1$), with $\delta_0 = (\sqrt{3}-1)/2$ (when $\delta_q = \delta_0$, $\kappa_{\rm f} = \kappa_{\rm t} = \kappa_{\rm s}$).

For $\delta_q = 0$ the interval reduces to $\kappa^* = 1$ and $\kappa_1 = \kappa_0 = 1$, $\bar{\kappa}_{-1} = -1$, and $\kappa_{-1} = \bar{\kappa}_{-2} = 0$. For $\delta_q = 1$, $\kappa^* \in [11/5, 11/4]$ and κ_0 reach a maximal value $\kappa_{0\mathrm{m}} = -1/5$ for $\kappa^* = 11/5$ ($\kappa_1 = 3/5$, $\kappa_{-1} = 0$, $\bar{\kappa}_{-1} = 1$, and $\bar{\kappa}_{-2} = -2/5$).

When $\delta_q = \delta_0$, the interval (55) is $[1, 2]$ and is the largest available. $\kappa^* = 1$ gives $\kappa_1 = 0$, $\kappa_0 = \bar{\kappa}_{-1} = 1$, $\kappa_{-1} = 3 - 2\sqrt{3}$, and $\bar{\kappa}_{-2} = 2(\sqrt{3} - 2)$; $\kappa^* = 3/2$ gives $\kappa_1 = \kappa_0 = \bar{\kappa}_{-1} = 1/2$, $\kappa_{-1} = 5 - 3\sqrt{3}$, and $\bar{\kappa}_{-2} = (6\sqrt{3} - 11)/2$; and $\kappa^* = 2$ gives $\kappa_1 = 1$, $\kappa_0 = \bar{\kappa}_{-1} = 0$, and $\kappa_{-1} = -\bar{\kappa}_{-2} = 7 - 4\sqrt{3}$.

Among the infinite set of functions $\kappa^*(\delta_q)$ which satisfy (55), we have chosen to use in section 5.2

$$\kappa^*(\delta_q) = 1 + \frac{15 + 4\sqrt{3}}{15}\delta_q - \frac{4\sqrt{3} - 3}{15}\delta_q^2 \,, \tag{56}$$

based on the following heuristic: the function $\kappa^*(\delta_q)$ is quadratic in δ_q, increasing, and goes through the points $(0, 1)$, $(\delta_0, 3/2)$, and $(1, 11/5)$.

3.6 Summary

Table 2 summarizes the results of the previous sections. Let us also recall the following results:

1. The linear LB equation with the bounce-back condition gives an exact Couette flow if the planes are parallel to the symmetry planes of the lattice and cut the non-perpendicular links in their middle. The same result applies for Poiseuille flows if Λ^2 is equal to some particular values: 1/4 if the flow is along the main axes.

2. The linear LB equation with the boundary conditions in Table 2, excepted the bounce-back one, gives the exact solution for any inclined Couette flow.

3. The linear LB equation with the multi-reflections gives the exact solution for any inclined Poiseuille flow.

4. Linear interpolations (24) and (25) are second-order accurate for general flows.

5. Multi-reflections with post-correction (46) are formally third-order accurate for general flows.

	BB	ULI	DLI	UQI	DQI	MR
δ_q	$\frac{1}{2}$	$\left[0, \frac{1}{2}\right]$	$\left[\frac{1}{2}, +\infty\right[$	$\left[0, \frac{1}{2}\right]$	$\left[\frac{1}{2}, 1\right[$	$[0, 1]$
κ_1	1	$2\delta_q$	$\frac{1}{2\delta_q}$	$\delta_q(1+2\delta_q^2)$	$\frac{1}{\delta_q(2\delta_q+1)}$	$\frac{\kappa^*\kappa_\mathrm{f}}{\kappa_\mathrm{s}} - 1$
κ_0	0	$1-2\delta_q$	0	$1-4\delta_q^2$	0	$2-\kappa^*$
κ_{-1}	0	0	0	$-\delta_q(1-2\delta_q)$	0	$\kappa_1 - \bar{\kappa}_{-2} - 1$
$\bar{\kappa}_{-1}$	0	0	$\frac{2\delta_q-1}{2\delta_q}$	0	$\frac{2\delta_q-1}{\delta_q}$	$2 - \frac{\kappa^*\kappa_\mathrm{t}}{\kappa_\mathrm{s}}$
$\bar{\kappa}_{-2}$	0	0	0	0	$-\frac{2\delta_q-1}{1+2\delta_q}$	$\frac{\kappa^*(\kappa_\mathrm{t}-2)}{\kappa_\mathrm{s}} - 1$
w_q	2	2	$\frac{1}{\delta_q}$	2	$\frac{2}{\delta_q(2\delta_q+1)}$	$\frac{4\kappa^*}{\kappa_\mathrm{s}}$
$F_{\bar{q}}^{\mathrm{p.c.}}$	0	0	0	0	0	$\frac{\kappa^*\Lambda^2\tilde{f}_q^{(2)}}{t_p^\star\nu\kappa_\mathrm{s}}$
κ_t	$3+2\delta_q$					
κ_s	$1+6\delta_q+4\delta_q^2$					
κ_f	$2(1+\delta_q)^2$					
	$\max\{1, \frac{\kappa_\mathrm{s}}{\kappa_\mathrm{t}}\} \leq \kappa^* \leq \frac{2\kappa_\mathrm{s}}{\kappa_\mathrm{f}}$					

	MR1	MR2
κ^*	$\frac{2\kappa_\mathrm{s}}{\kappa_\mathrm{f}}$	$\frac{1}{15}\left(15 + (15+4\sqrt{3})\delta_q - (4\sqrt{3}-3)\delta_q^2\right)$

Table 2: Valid range for δ_q and coefficients κ_1, κ_0, κ_{-1}, $\bar{\kappa}_{-1}$, $\bar{\kappa}_{-2}$, w_q, and $F_{\bar{q}}^{\mathrm{p.c.}}$ for the different boundary conditions; BB: bounce-back, ULI: upwind linear interpolation, DLI: downwind linear interpolation, UQI: upwind quadratic interpolation, DQI: downwind quadratic interpolation, MR: multi-reflection.

4 Momentum transfer on the boundary

4.1 Classical definition

Let us define the momentum transport $\vec{M}^{(\mathrm{c})}$ on the boundary in the classical way (see [14, 22]) as:

$$\vec{M}^{(\mathrm{c})} = \sum_{q\in\mathcal{C}} (\tilde{f}_q(\vec{r}_\mathrm{b})\vec{c}_q - f_{\bar{q}}(\vec{r}_\mathrm{b})\vec{c}_{\bar{q}}) = \sum_{q\in\mathcal{C}} (\tilde{f}_q(\vec{r}_\mathrm{b}) + f_{\bar{q}}(\vec{r}_\mathrm{b}))\vec{c}_q \ , \tag{57}$$

where the sum goes through all the cut links $q \in \mathcal{C}$ for all the boundary nodes $\vec{r}_\mathrm{b}$. Let us denote

$$M_q(\vec{r}) = \tilde{f}_q(\vec{r}) + f_{\bar{q}}(\vec{r}) \ , \tag{58}$$

the sum of equations (A.1) and (A.2) gives

$$M_q(\vec{r}) = t_p^\star \left(2P + \frac{3j_q^2 - j^2}{\tilde{\rho}} + F_q \right) + (2-\lambda_\nu) f_q^{(1)} - \lambda_2 f_q^{(2)} \ . \tag{59}$$

Using equations (26) and (27) and the projected stationary Navier-Stokes equation (49), it comes

$$\begin{aligned} M_q(\vec{r}) &= t_p^\star \left(2P + \frac{3j_q^2 - j^2}{\tilde{\rho}} - 6\nu\partial_q j_q \right. \\ &\qquad \left. + \partial_q P + \partial_q \frac{3j_q^2 - j^2}{2\tilde{\rho}} - 3\nu\partial_{qq} j_q \right) \ , \\ &= M_q^{(\mathrm{b})}\left(\vec{r} + \frac{1}{2}\vec{c}_q \right) \ , \end{aligned} \tag{60}$$

where $M_q^{(\mathrm{b})}(\vec{r})$ is defined as

$$M_q^{(\mathrm{b})}(\vec{r}) = 2t_p^\star \left(P + \frac{3j_q^2 - j^2}{2\tilde{\rho}} - 3\nu\partial_q j_q \right) , \tag{61}$$

the right hand side term being taken at $\vec{r}$.

If the pressure, non-linear terms and momentum derivatives are constant for all $\vec{r}_\mathrm{b} + \vec{c}_q/2$, they can be factored in eq. (57) to give

$$\vec{M}^{(\mathrm{c})} = \left(P - \frac{j^2}{2\tilde{\rho}} \right) \sum_{q\in\mathcal{C}} 2t_p^\star \vec{c}_q + \left(\frac{j_\alpha j_\beta}{2\tilde{\rho}} - \nu\partial_\beta j_\alpha \right) \sum_{q\in\mathcal{C}} 6t_p^\star c_{i\alpha} c_{i\beta} \vec{c}_q \ . \tag{62}$$

For a plane surface going through the points A_{00}, $\mathrm{A}_{10} = \mathrm{A}_{00} + (l_x, 0, l_z)$, and $\mathrm{A}_{01} = \mathrm{A}_{00} + (0, m_y, m_z)$, where l_x, l_z, m_y, and m_z are integers, it can be shown that

$$\begin{aligned} \sum_{q \in \mathcal{C}_\mathrm{S}} 2 t_p^\star \vec{c}_q &= A_\mathrm{S} \vec{n} \ , \\ \sum_{q \in \mathcal{C}_\mathrm{S}} 6 t_p^\star c_{i\alpha} c_{i\beta} c_{i\gamma} &= A_\mathrm{S} (n_\alpha \delta_{\beta\gamma} + n_\beta \delta_{\alpha\gamma} + n_\gamma \delta_{\alpha\beta}) \ , \end{aligned} \tag{63}$$

where $\vec{n}$ is the normal to the surface directed outwards, A_S is the area of the plane surface limited by $S = (\mathrm{A}_{00}, \mathrm{A}_{10}, \mathrm{A}_{11}, \mathrm{A}_{01}, \mathrm{A}_{00})$ (with $\mathrm{A}_{11} = \mathrm{A}_{00} + (l_x, m_y, l_z + m_z)$), and $\mathcal{C}_\mathrm{S}$ is the set of links cut by S. It follows (using $\nabla \cdot \vec{j} = 0$) that $\vec{M}^{(\mathrm{c})}$ restricted to S is given by the classical formula for incompressible flows

$$\vec{M}_S^{(\mathrm{c})} = A_\mathrm{S} \left(P \vec{n} + \frac{j_n \vec{j}}{\tilde{\rho}} - \nu (\partial_n \vec{j} + \nabla j_n) \right) \ , \tag{64}$$

where $j_n = \vec{j} \cdot \vec{n}$ and ∂_n is the derivative along the normal to the surface.

When the external force is constant and the flow is stationary, it follows from the momentum conservation that

$$\vec{M}^{(\mathrm{c})} = \vec{F} V^l \ , \tag{65}$$

where V^l is the number of nodes where the force addition $t_p^\star \ \vec{c}_i \cdot \vec{F}$ is applied in equation (2). Consequently, $\vec{M}^{(\mathrm{c})}$ is independent of the solution when an external force $\vec{F}$ is used.

4.2 New definition

Let us now give a new definition of the momentum transport on the boundary

$$\vec{M}^{(\mathrm{n})} = \sum_{q \in \mathcal{C}} M_q^{(\mathrm{b})} (\vec{r}_\mathrm{b} + \delta_q \vec{c}_q) \vec{c}_q \ , \tag{66}$$

where $M_q^{(\mathrm{b})} (\vec{r}_\mathrm{b} + \delta_q \vec{c}_q)$ can be computed as

$$M_q^{(\mathrm{b})} (\vec{r}_\mathrm{b} + \delta_q \vec{c}_q) = \left(\frac{1}{2} + \delta_q \right) M_q (\vec{r}_\mathrm{b}) + \left(\frac{1}{2} - \delta_q \right) M_q (\vec{r}_\mathrm{b} - \vec{c}_q) \ . \tag{67}$$

Indeed relation (67) comes from the following property of any function $f(x)$

$$f(x+\delta) \approx \frac{1}{2}\left((1+2\delta)\, f\Big(x+\frac{1}{2}\Big) + (1-2\delta)\, f\Big(x-\frac{1}{2}\Big)\right). \tag{68}$$

With the new definition the momentum exchange is computed on the surface with a second-order accuracy and not in the middle of the cut links as for the classical definition. The difference between the first and second definitions is

$$\vec{M}^{(\mathrm{n})} - \vec{M}^{(\mathrm{c})} = \sum_q \left(\delta_q - \frac{1}{2}\right) \partial_q M_q^{(\mathrm{b})}(\vec{r}_{\mathrm{b}})\, \vec{c}_q \ . \tag{69}$$

Note that the new definition does not verify eq. (65), in a way similar to the non-conservation of mass by the interpolation and multi-reflection schemes (see appendix B for examples).

5 Numerical results for static boundaries

5.1 Stokes flow

5.1.1 Numerical set-up

In order to test accuracy of the different boundary conditions, we compare first the results with the quasi-analytical solutions of the stationary Stokes equation (12). At a *macroscopic* level with respect to the level of the Stokes equation, the flow of a single fluid in a porous medium is well described by the Darcy's Law which relates the flow rate of the fluid $\vec{Q}$ to the applied forcing across the medium in a linear way:

$$\vec{Q} = \frac{1}{\nu}\mathsf{K}(\overline{-\nabla P + \vec{F}}) \ , \tag{70}$$

where K is the permeability tensor the porous medium and $\overline{\nabla P}$ is the mean value of the pressure gradient across it. The flow rate $\vec{Q}$ is usually computed as a volume mean value of the momentum $\vec{j}$:

$$\vec{Q} = \frac{1}{\tau_0}\sum_{\vec{r}} \vec{j}(\vec{r}) \ . \tag{71}$$

Here, the summation goes through all the points in the computational domain and τ_0 is equal to a volume of the sample. It can be shown that when the

momentum is redefined as in rel. (9), $\vec{Q}$ coincides with the mean centered population mass flux $\vec{\Phi}$:

$$\vec{\Phi} = \frac{1}{\tau_0} \sum_{\vec{r}} \vec{\Phi}^{\mathrm{p}}(\vec{r}) \ , \tag{72}$$

$$\Phi^{\mathrm{p}}_{\alpha}(\vec{r}) = \frac{1}{2} \sum_{q=1}^{b_m} (\tilde{f}_i(\vec{r}) + f_i(\vec{r})) c_{i\alpha} \ . \tag{73}$$

One should keep in mind, however, that expression (71) and (72) represent crude integration rules which do not take into account the exact boundary position. The permeability can also be derived from the drag $\vec{F}^d$ on the solid

$$\vec{F}^d = -(\overline{\nabla P - \vec{F}}) \ . \tag{74}$$

and approximated by the momentum transport $\vec{M}^{(\mathrm{c})}$ or $\vec{M}^{(\mathrm{n})}$ on the boundary as defined in (57) or (66).

When the fluid is forced in a given direction α, and $\overline{\nabla P} = 0$ (e.g. periodic porous media), the diagonal terms of the permeability tensor K can be computed as

$$k_{\alpha\alpha} = \frac{\nu Q_\alpha}{\overline{F_\alpha}}, \qquad \overline{\nabla P} = 0 \ . \tag{75}$$

In the following sections the main flow is in z-direction and the permeability k_{zz} is simply denoted k. For the simulations with an external force (sections 5.1.4, 5.1.5, and 5.2) only the permeability k in periodic samples is given. For the simulations without external force (section 5.1.6) the results are given for both the $\vec{Q}$ as defined in (71), and the drag force $\vec{M}^{(\mathrm{c})}$ as defined in (57). The relative error for any scalar LB variable s_{lb} with respect to its reference value s_{a} is computed as

$$E^{(\mathrm{r})}_h(s_{\mathrm{lb}}) = \frac{s_{\mathrm{lb}}}{s_{\mathrm{a}}} - 1 \ , \tag{76}$$

where the subscript h corresponds to the grid spacing, *i. e.* the inverse of the number of grid points. Because of the integration errors inherent to the relations (71), (72), and (57), these global measurements are affected not only by the errors coming from the LB method and the boundary discretization, but also by these integration errors. We also compare the solutions obtained

for the velocity or pressure fields with their reference solutions. The difference between the LB solution for $s_{\rm lb} = \{u_y, u_z, P\}$ and the quasi-analytical solution $s_{\rm a}$ for the same field is computed in L^2 norm:

$$E^{(2)}(s_{\rm lb}) = \sqrt{\sum (s_{\rm lb} - s_{\rm a})^2 / \sum s_{\rm a}^2}\,, \tag{77}$$

where the sums are taken either over all the boundary points ('b' subscripts) or over the fluid points on the whole grid.

Let us remind once more, that the simulations at fixed value Λ^2 guarantee the linearity of the the LB Stokes solution (11) with respect to $\vec{F}/\nu$ for the bounce-back reflection and multi-reflection with post correction (51). For these boundary conditions the results are given for one value of the viscosity only. With other boundary conditions, the exact position of boundary at second and/or higher orders still changes with the viscosity, leading to abnormal dependency of the permeability on the viscosity. The corresponding error reduces when $\nu \to 0$, but the computation time to reach the steady state increases then accordingly.

5.1.2 Couette and Poiseuille flows

As it was said in the sections 3.3 and 3.4, Couette and Poiseuille flows must lead to exact solutions for the **linear** LB equation. For the bounce-back, linear and quadratic interpolations, this is possible only when the flow is along the symmetry axes of the lattice and the walls are located at their effective place (set for Poiseuille flows by the values of λ_ν and λ_2, Λ^2 for the bounce-back rule, see eq. (5.1.2)). For the multi-reflections given in section 39 this is true for any inclination of the flows with respect to the axes and any value of λ_ν and λ_2

We do not want to unduly increase the length of the document with results showing only round-off errors and we ask the reader to take our words that we have checked and rechecked these results (for at least ten years for some of them). If the reader is unable to reproduce them, there are only the following possibilities left:

- We have not been clear enough in our presentation.
- We have left some typos in the text or/and the formulae.
- The forcing term is not exactly implemented as in (2) or/and the momentum is not redefined as in (9) with $I_{\rm f} = -1/2$ (as in [14]).

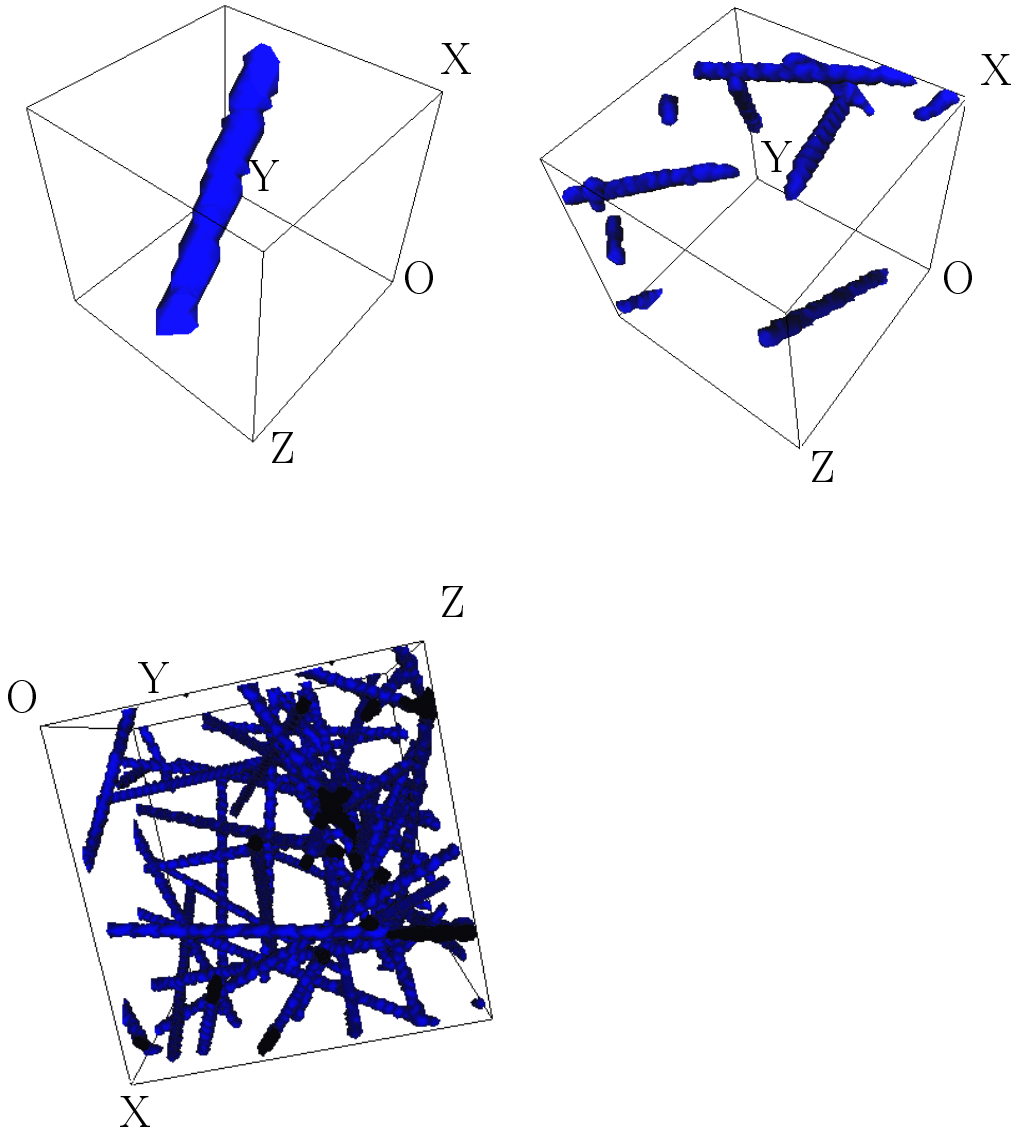

Figure 2: Fiber materials, from left to right and top to bottom: a) porosity $\phi \approx 0.965$ in a 20^3 box, b) porosity $\phi \approx 0.973$ in a 50^3 box, c) porosity $\phi \approx 0.941$ in a 90^3 box.

- The equilibrium distribution is not linear in momentum.
- There is (are) bug(s) in his program.

In our opinion, the merit of these academic flows is first to illustrate our approach in a simple way, secondly to provide simple tests of the computer implementation of boundary conditions.

5.1.3 Flow around random fibers

In order to illustrate the benefit of using a constant value of Λ^2 in a non-trivial case, we use models of periodic fibrous material shown in Figures 2a to c. The fiber web consists of overlapping cylinders (a single fiber for Fig. 2a). of radius equal to 2 lattice unit. The distribution of the cylinder axes is obtained from a Poisson line process [29]. The measurements are performed with a $D3Q15$ model having one eigenvalue λ_ν for all the even moments and one for all the odd moments (λ_2); the forcing is $F = 2 \times 10^{-6}$ and the boundary condition is the bounce-back rule. We give in Table 3 first the permeability k_{xx} obtained for the three samples with $\nu = 1/6$ and $\Lambda^2 = 1/4$, then the relative difference in permeability for the case $\Lambda^2 = 1/4$ and for the BGK case ($\lambda_2 = \lambda_\nu$), with $k^{\text{rel.}}(\lambda_\nu)$ given by

$$k^{\text{rel.}}(\lambda_\nu) = \frac{k_{xx}(\lambda_\nu) - k_{xx}(1)}{k_{xx}(1)} \,, \tag{78}$$

where $k_{xx}(1)$ is the value of k_{xx} for $\lambda_\nu = 1$ (the choice $\lambda_\nu = 1$ being rather arbitrary).

First we do not want let the reader believe that we measure the permeability of the samples with an accuracy of few 10^{-13}. We only claim that the viscosity can change by a factor 60 without changing the measured permeabilities by more than $\pm 3 \times 10^{-12}$ when using a constant value of Λ^2. This is to be contrasted with the BGK case where the permeability is rapidly increasing with the viscosity (by more than a factor five) as expected form the results for Poiseuille flows. This behavior of the BGK model is in a total contradiction with the physics of Stokes flows.

Finally the results have been obtained for a convergence criteria based on the relative difference between the maximum and minimum mass flux, the computation ending for a relative difference less than 10^{-6}. Although this criteria is quite stringent, it probably accounts for the 10^{-12} error in

ν	λ_ν	20^3, $\phi \approx 0.965$		50^3, $\phi \approx 0.973$		90^3, $\phi \approx 0.941$	
		k_{xx}		k_{xx}		k_{xx}	
1/6	1	34.0659875		42.249358		26.150806	
		$k^{\text{rel.}}$		$k^{\text{rel.}}$		$k^{\text{rel.}}$	
		$\Lambda^2=1/4$	BGK	$\Lambda^2=1/4$	BGK	$\Lambda^2=1/4$	BGK
		$\times 10^{-12}$		$\times 10^{-12}$		$\times 10^{-12}$	
1/24	8/5	0.1	−0.077	0.1	−0.094	0.1	−0.083
1/6	1	0	0.016	0	0.021	0	0.018
1/2	1/2	0.5	0.311	1.1	0.356	−	−
7/6	1/4	1.3	1.243	−0.3	1.123	−	−
5/2	1/8	−2.8	4.699	0.3	2.946	−0.1	2.236

Table 3: The third line gives the permeability of the three fiber samples shown in Figs. 2a to c for $\nu = 1/6$. The bottom of the table gives the relative permeability with respect to the previous values for $\Lambda^2 = 1/4$ and the BGK model.

the permeability measurements (this error is a few order of magnitude larger than the numerical round-off ones).

5.1.4 Cubic array of spheres

The solution for a viscous flow past a cubic array of spheres [30, 31] shows that the drag force F^d on the sphere, exerted by the fluid moving with the average speed $\overline{U}$ depends on the relative volume solid concentration c as

$$F^d = \frac{6\pi\mu a\overline{U}}{k^\star(\chi)} , \qquad k = \frac{\tau_0}{6\pi a}k^\star , \qquad \chi = (c/c_{\max})^{1/3} , \tag{79}$$

where a is the sphere radius and $c_{\max} = \pi/6$ is the maximal concentration. The function $k^\star(\chi)$, inverse of the nondimensional drag, is tabulated in Table 4.9 of [32]. For dense array, we use their results (b).

We computed the permeability from relations (71) and (75) and tested the boundary conditions (23), (24), (25), and (51). The external force is $F = 2 \times 10^{-5}$. The results in tables 4 and 5 show the relative permeability error with respect to the reference value computed from (79) and [32]. The permeabilities in table 4 were obtained for $\tau = 2$, but are independent of the viscosity. Since this no longer the case for the linear interpolations (24)

	bounce-back		Multi-reflection	
χ	$E^{(\mathrm{r})}(k)[\%]$	$n/100$	$E^{(\mathrm{r})}(k)[\%]$	$n/100$
0.5	−1.02	21	−0.42	22
0.6	−2.96	13	−0.46	15
0.7	−2.12	9	−0.44	10
0.85	1.50	5	−0.35	19
0.90	−4.38	4	−0.67	4
0.95	−4.28	3	−0.56	5

Table 4: Comparison of the relative errors on permeability for a cubic array of spheres and the bounce-back and multi-reflection boundary conditions in a 25^3 box.

and (25), the corresponding results are given for $\tau = 2$ and 0.6 in Table 5. The tables include the number of time steps n required to reach a change in k less than 10^{-6} between 10^3 time steps. Note that for the linear interpolations, decreasing the viscosity by a factor 15 increases both the accuracy and the convergence time by almost the same factor.

	$\tau = 2$		$\tau = 0.6$	
χ	$E^{(\mathrm{r})}(k)[\%]$	$n/100$	$E^{(\mathrm{r})}(k)[\%]$	$n/100$
0.5	4.28	20	0.88	330
0.6	3.38	14	0.32	230
0.7	3.61	9	0.38	150
0.85	7.73	5	1.68	80
0.90	8.67	4	0.65	70
0.95	10.27	3	1.084	60

Table 5: Comparison of the relative errors on permeability for a cubic array of spheres and the linear boundary conditions for $\tau = 2$ and 0.6 in a 25^3 box.

Note that for the two most dense arrays, situations where some boundary nodes have only one fluid neighbor appear. Despite that, higher accuracy is maintained with the multi-reflection with post correction for all solid fractions.

Although the precision of the linear interpolations in this test is quite satisfactory for small viscosities, it deteriorates when the gap between the

spheres approaches 1-2 lattice units. Besides that, the computational time is then $10-20$ times higher than for multi-reflection with post correction.

5.1.5 Square array of cylinders

For a periodic square array of cylinders, the force exerted on the cylinders per unit length is (see [30, 32, 33])

$$\frac{F^d}{l} = \frac{4\pi\mu\overline{U}}{k^\star(c)}\,, \qquad k = \frac{\tau_0}{4\pi l}k^\star\,, \tag{80}$$

where l is the cylinder length and c is the relative solid square fraction ($c_{\max} = \pi/4$). The function $k^\star(c)$ is tabulated in Table 4.12 of [32].

		Bounce-back	Linear	Multi-reflection
c	r	$k^{\text{rel.}}(\%)$	$k^{\text{rel.}}(\%)$	$k^{\text{rel.}}(\%)$
0.2	8.326	-4.49	-0.04	-0.35
0.3	10.198	-2.59	0.04	-0.35
0.4	11.775	-0.48	1.76	0.05
0.5	13.165	-17.51	-1.36	-0.99
0.6	14.422	-15.56	0.70	-0.45
0.7	15.577	-6.88	22.49	7.50

Table 6: Comparison of the relative errors on permeability for a square array of cylinders and the bounce-back, linear and full multi-reflection boundary conditions on a 33^2 grid, r is cylinder radius.

Simulations are similar as above; they are terminated when a change in k is less than 10^{-10} between 10^3 time steps. All computations are done with $\tau = 0.875$, $\lambda_2 = -1$ (corresponding to (42)). The results with the boundary conditions in the form (23), (24), (25), and (51) are shown in Tables 6 and 7 for periodic cells 33^2 and 99^2, accordingly.

The results with the coefficients (51) but without the post correction (46) and with the coefficients (6) from [14] are shown in Table 8. We would like to stress that they are similar to the results obtained with the linear interpolations.

c	r	Bounce-back	Linear	Multi-reflection
0.2	24.979	1.08	0.15	−0.01
0.3	30.593	−0.73	0.09	0.03
0.4	35.326	−1.43	0.04	−0.02
0.5	39.495	−2.83	0.05	−0.03
0.6	43.265	−5.27	0.02	−0.11
0.7	46.732	0.79	3.79	0.31
0.75	48.372	−27.18	6.08	0.79

Table 7: Similar to Table 6 for a 99^2 grid.

c	Multi-reflection without correction, $E^{(\mathrm{r})}(k)[\%]$	Interpolation (6) from [14] $E^{(\mathrm{r})}(k)[\%]$
0.2	0.68	0.86
0.3	0.51	0.92
0.4	2.16	2.09
0.5	1.41	2.97
0.6	5.28	5.47
0.7	35.93	28.63

Table 8: Comparison of the relative errors on permeability for a square array of cylinders and the multi-reflection without the post-correction and the quadratic interpolation boundary conditions on a 33^2 grid.

5.1.6 Cylinder between moving flat walls

The flow configuration is similar to [34]. The box is periodic in the x- and z-directions. Its dimension is $l \times W \times L$. The axis of the cylinder is along the x-axis and cut the $x = 0$ plane at (y_0, z_0) referred below as the "center" of the cylinder; the flat boundaries are found at $y = \pm H$ and are moving in the z-direction with velocity $-\vec{u}_{\mathrm{w}}$. This set-up simulates a periodic flow in z-direction past an array of cylinders at rest between moving parallel planes. Multi-pole solution to this problem is discussed in Appendix A. Pressure/velocity/stream function solution is compared with the quasi-analytical solution. The lattice Boltzmann results are obtained with the same parameters as for periodic array of cylinders. The distance δ_q between the flat boundaries and their boundary nodes is put equal to 0.5.

The relative errors of the force and seepage velocity are given in Table 9.

c	Bounce-back		Linear		Multi-reflection	
0.2	2.14	-1.91	7.2×10^{-2}	-0.12	2.6×10^{-2}	-0.11
0.3	1.33	-1.12	5.6×10^{-2}	-0.17	4.8×10^{-2}	-0.21
0.4	-0.43	0.21	-0.71	0.60	-0.19	8.4×10^{-3}
0.5	8.22	-7.91	0.59	-0.93	8.3×10^{-2}	-0.61
0.6	6.14	-6.67	-0.13	-0.15	-0.69	0.16
0.7	0.95	-1.68	1.10	-1.76	5.56	6.39

Table 9: Relative error (in %) of the force (left columns) and seepage velocity (right columns) for a square array of cylinders between moving flat walls and the bounce-back, linear and full multi-reflection boundary conditions on a 33^2 grid and $\tau = 0.875$.

The errors are below 10%, even for the bounce-back condition, most of them are below 1% especially for the linear interpolation and the multi-reflection conditions. As for a periodic array of cylinders, it happens first at the concentration 0.6 that a boundary point lacks one point to perform multi-reflection in a full form. At the concentration 0.7, in addition, some boundary cells are intersected by both boundaries (flat wall and the cylinder). We have found that the coefficients (56) are more stable in this situation than the coefficients (51). Since the accuracy of the coefficients (56) depends on the viscosity, we have chosen here to use bounce-back condition on a flat wall combined with multi-reflection on the cylinder for $c = 0.7$. In this way, multi-reflection/bounce-back solution is still controlled by Λ^2, but its errors in flow direction (force, seepage velocity and u_z) become larger than the error of linear interpolation. Finally, for $c = 0.7$, $r = 15.57$ here and in the previous test, bounce-back condition works surprisingly well. Indeed, when the curvature of the cylinder is small, the flow in a gap is close to Poiseuille flow (in the previous test) and to Couette flow (in current test). Moreover, here the cylinder boundary is shifted at approximately $\delta_q = 1/2$ from the last boundary nodes $y = \pm 16$ (since $r = 15.57$ and cylinder center $y_0 = 0$). While applied with $\Lambda^2 = 1/4$, bounce-back and linear interpolation give then quite good results.

The Table 10 summarizes the results for the pressure and the z and y components of the momentum. These results based on the norm (77) of the error are confirmed by a more detailed study of the difference between the lattice Boltzmann and the quasi-analytical solution. The errors between the

c	Bounce-back		Linear		Multi-reflection	
	Pressure					
0.2	13.5	8.6	4.9	3.6	4.2	3.4
0.3	21.2	12.1	6.1	4.0	3.6	3.2
0.4	20.4	15.1	6.5	6.1	3.9	3.9
0.5	19.0	16.5	2.5	2.5	3.5	3.5
0.6	7.5	6.2	6.1	5.7	7.1	6.8
0.7	32.4	28.7	32.0	28.3	30.2	26.7
	Momentum in the z-direction					
0.2	19.8	1.86	1.15	0.09	0.49	0.04
0.3	17.2	1.47	1.38	0.15	0.55	0.05
0.4	17.5	1.59	5.82	0.75	1.39	0.20
0.5	24.7	6.59	2.85	0.59	1.02	0.24
0.6	16.1	5.17	3.18	1.20	2.24	1.07
0.7	9.8	5.32	8.86	4.64	13.12	6.67
	Momentum in the y-direction					
0.2	20.3	10.8	5.0	1.6	2.4	0.9
0.3	47.7	21.9	5.2	2.3	2.2	0.9
0.4	34.6	27.4	8.9	7.0	3.2	2.2
0.5	39.0	26.1	7.0	3.5	3.9	2.3
0.6	30.6	15.9	9.8	5.2	6.6	4.4
0.7	26.1	14.3	17.5	8.9	13.9	7.1

Table 10: Relative error (77) of the pressure and the momentums in the z and y directions (in %) for the parameters given in Table 9. Left columns: boundary nodes and right columns: bulk.

LB results and the reference solution at the boundary points as a function of their angular position for $c = 0.4$ are plotted in Figure 3 for the pressure and velocity fields. The streamlines are plotted in Figures 4a ($c = 0.4$) and 4b ($c = 0.5$). The integration of the velocity fields is done in a similar way for all LB techniques and quasi-analytical solution.

All the simulations reported above have been done in a fully symmetric numerical set-up. The LB lift force is then equal to zero and no total mass violation happens with the boundary interpolations. When the center of the sphere/cylinder is shifted from the cell center along the flow direction, these properties do not hold any more. As an example, let us move the cylinder

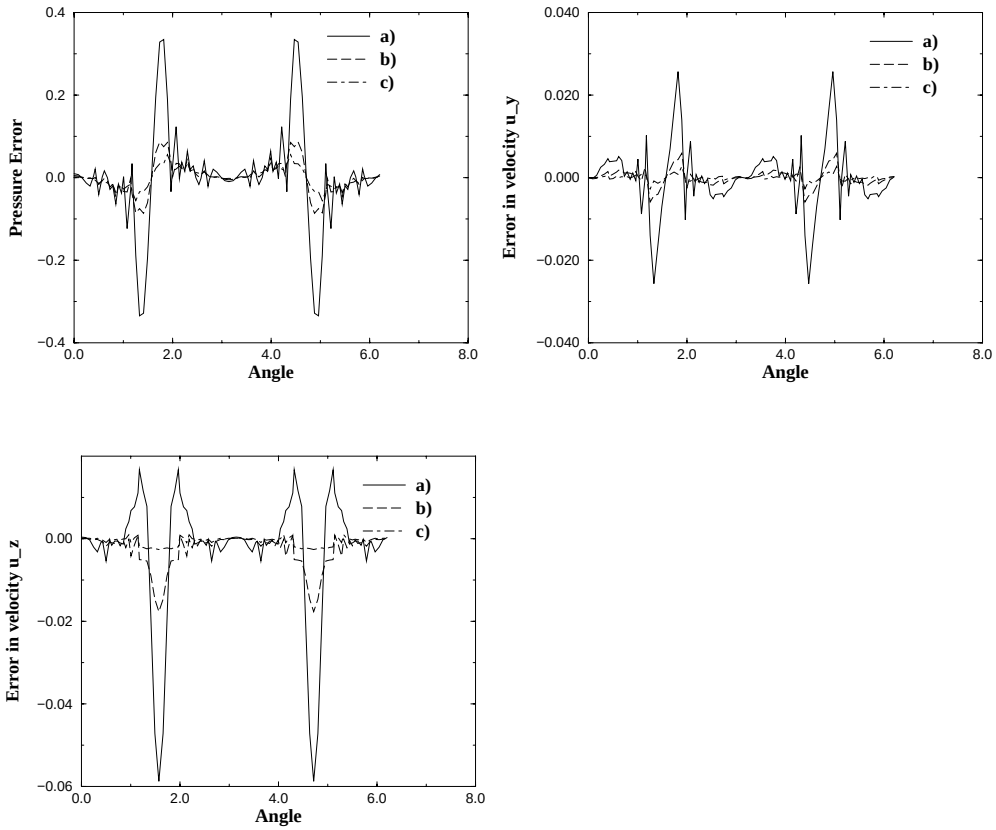

Figure 3: Error between the LB results and quasi-analytical solution at the boundary points for $c = 0.4$; a) bounce-back, b) linear interpolation, c) multi-reflection. Left to right: pressure rescaled by its max value, y- and z-velocity components rescaled by u_{w}. The data corresponds to streamlines in Figure 4.

center from the symmetric position on the node $(y_0, z_0) = (18, 15)$ to a final position $(y_0, z_0) = (18, 15.48)$ close to the middle of a link, with an step increment $(\delta_y, \delta_z) = (0, 0.04)$. The box size is 33^2 and the cylinder radius is $R = 12$ ($c \approx 0.42$). Figure 5 plots the corresponding mass loss per time step for the linear interpolation and multi-reflection with post correction (there is no mass loss for the bounce-back condition). We see that multi-reflection with post correction has on average a smaller mass loss than the linear interpolation.

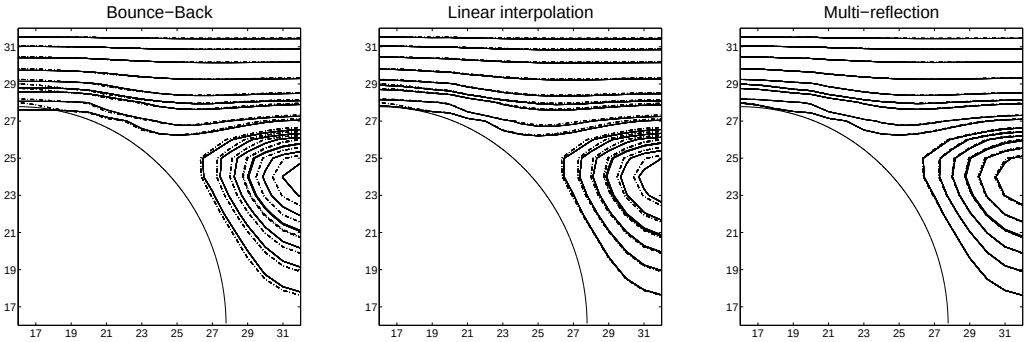

a) $c = 0.4$

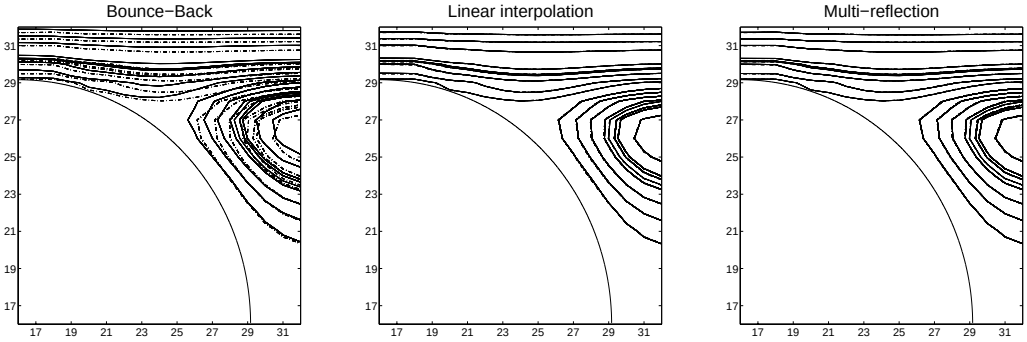

b) $c = 0.5$

Figure 4: Streamlines for the flow around a cylinder between flat walls for $c = 0.4$ (a) and $c = 0.5$ (b). Left to right: bounce-back method, linear interpolation and multi-reflection (solid lines) compared to the quasi-analytical solution (dashed lines).

Figure 6 shows the relative error in drag force, using its value for the symmetric case $(y_0, z_0) = (18, 15)$ as reference. The multi-reflection with post correction is much more accurate than bounce-back, and the accuracy for the linear interpolation is usually found between bounce-back and multi-reflection. Note that by definition the error for $(y_0, z_0) = (18, 15)$ is zero and far away from the values displayed in figure 6: respectively 8%, 2%, and 0.15% for bounce-back, linear interpolation, and multi-reflection. Such large values are surprising *a priori*, but we think their explanation is the following. When $(y_0, z_0) = (18, 15)$, in our simulations the points $(6, 15)$ and $(30, 15)$ are considered as solid points of the cylinder; the corresponding links in the

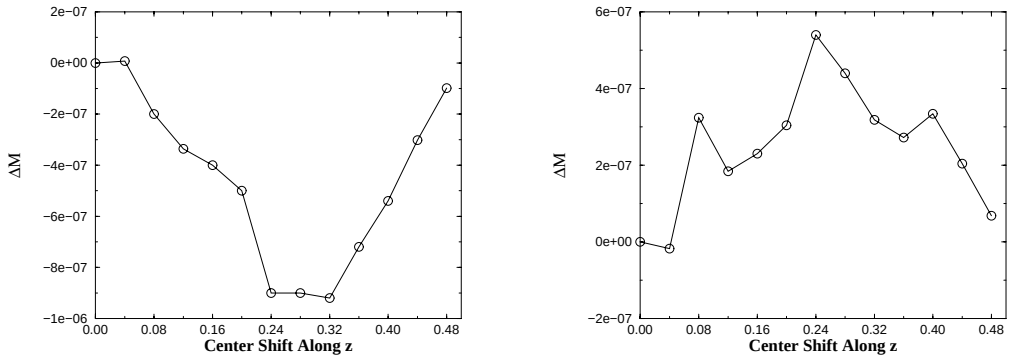

Figure 5: Mass loss per time step at stationary regime corresponds to the previous picture. Left: linear interpolation. Right: multi-reflection with post correction.

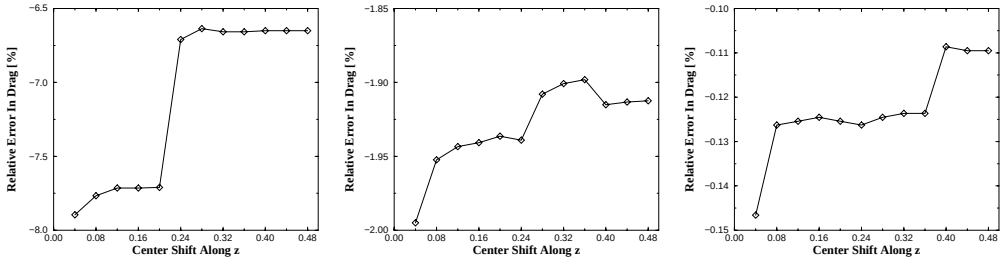

Figure 6: Relative difference in drag with respect to symmetric cylinder position when its center is shifted along z-axis. Left to right: bounce-back, linear interpolation, multi-reflection with post correction.

z-direction are then cut by the boundary (for instance $(30, 15)$ to $(30, 16)$). When the cylinder center is shifted by a non-zero multiple of (δ_y, δ_z), these nodes become fluid ones (boundary nodes). The links which were cut in the symmetric case now connect two fluid nodes and are considered as fluid links, although some of them are tangent to the cylinder (for instance $(30, 15)$ to $(30, 16)$). In our opinion, figure 6 illustrates the order of magnitude of the errors caused by a too simple treatment of the links tangent to the boundary surface. It should be noted that multi-reflection with post correction reduces considerably the error (an order of magnitude compared to the linear interpolation). A better treatment of these links is left for future work.

5.1.7 Summary for Stokes flows

As an attempt to extract some convergence factor, we give in Table 11 the convergence factor $K^2_{nh,h} = n^{-2}E^{(\mathrm{r})}_{nh}(k)/E^{(\mathrm{r})}_{h}(k)$ for the square array of cylinders (section 5.1.5). A formal second-order accuracy in the permeability calculations should correspond to $K^2_{nh,h}(k) = 1$. The convergence factors are rather disperse and their values do not reflect the convergence behavior when the coarse grid errors change their sign and/or when they are very close to zero. Note that including the data of Table 12 does not help.

c	Bounce-back	Linear	Multi-reflection
0.2	−0.46	−0.03	2.65
0.3	0.40	0.05	−1.48
0.4	0.04	4.82	−0.32
0.5	0.69	−3.25	3.60
0.6	0.33	3.21	0.46
0.7	−0.97	0.66	2.65

Table 11: Convergence estimator $K^2_{nh,h}$ for the data in Tables 6 and 7.

In our opinion the best illustration of the difficulties to get convincing convergence factors is given by the figure 6 of reference [14]. It shows that the observed dispersion of the global errors is very large, even for a very extensive numerical test. It seems to us that linear resolutions at least an order of magnitude smaller than ours (three orders more computer time) would be required in order to obtain unquestionable convergence factors. As stated in the introduction, our goals were set in the context of moderate resolutions and/or moving boundaries and not in the academic context of convergence factor for an infinite number of grid points.

Despite the difficulties to demonstrate obvious convergence factors, we hope to have shown in a convincing way that the results given in the tables and figures of the previous sections share the following trends:

1. The errors are significantly smaller for the bulk than for the boundary points, which support our assumption that the errors are mostly due to the boundary conditions rather than to the approximation of the Stokes equation by the lattice Boltzmann scheme itself.

2. The errors are significantly larger for the pressure and the y component of the momentum than for the z component of the momentum.

3. Pressure/velocity fluctuations obtained with the bounce-back rule near the cylinder boundary are similar to those described in [10] for inclined Poiseuille flow. The oscillations are considerably smoothed by linear interpolations and still more by the multi-reflection.

4. The linear interpolation improves the overall accuracy by almost an order of magnitude compared to the bounce-back condition, while an additional factor two is achieved when the full the multi-reflection condition is available, *i. e.* when $c \leq 0.6$ for which the channel width is larger than three ($c < 0.6$ for the 33^2 case).

5. Although the results obtained with linear interpolation can be further improved by decreasing the viscosity, the corresponding computational time is increased quite significantly.

6. Bounce-back condition provides very satisfactory results for tangential velocity when the flow is dominated by the flow in very narrow straight channels and Λ^2 is fixed close to the value $1/4$ (which gives the exact Poiseuille solution).

5.2 Navier-Stokes flow in a square array of cylinders

The flow configuration here is the same as in section 5.1.5. Navier-Stokes equilibrium (6) is applied in its incompressible variant [20, 21]. Solution for a 66^2 box is computed at solid fractions $c \in \{0.2, 0.6\}$ for Re numbers in the range $[0, 180]$. This interval has been chosen for comparison with the results computed using stationary finite element (FE) method in [35] and with non-stationary FE method in [36]. Note that these two sets of results differ significantly for $c = 0.5$ and $c = 0.6$ (see figure 8). According to Ghaddar [36], these differences may come from "a lack of resolution due possibly to large iteration or/and discretization errors" in [35]. We have also observed a quite strange feature in the data of their table I: for any Reynolds number the permeabilities for $c = 0.5$ are exactly those for $c = 0.6$ divided by 0.291 (up to the table accuracy). LB method with bounce-back reflection is also used to simulate this flow in [37].

c	Finite-Element [35]	Bounce-back	Linear	Multi-reflection
0.2	2.54	-1.63	5.5×10^{-2}	-6.5×10^{-2}
0.3	0.53	0.78	0.51	2.8×10^{-2}
0.4	-0.64	-4.86	0.13	-9.2×10^{-2}
0.5	-2.54	-1.1	-0.95	-8.9×10^{-3}
0.6	-8.36	-6.9	0.55	-2.1×10^{-1}

Table 12: Relative permeability error (in %) for the Stokes regime with respect to the reference value (80).

Table 12 gives for this grid size the relative error $E^{(\mathrm{r})}(k)$ of the Stokes permeability k_S with respect to the reference values computed from (80) and [32]. The Stokes solution is obtained with $\Lambda^2 = 1/4$ and the solution (42) at $\tau = 1$.

The dimensionless permeabilities are scaled below by the quasi-analytical solution [33] in the Stokes regime, except the results of Ghaddar which are scaled by its own Stokes values, being believed "virtually exact" (see Table V in [36]). They are plotted in Figure 7 for $c = 0.3$ and 0.5. For these fractions, bounce-back solution at Stokes regime has a relatively small error (see in Table 12). We find then that the Navier-Stokes results are also rather close together for the three boundary techniques. For $c = 0.4$, the bounce-back results differ significantly from those obtained with the linear interpolations and multi-reflections. Figures 8 show for each method the effect of scaling the apparent permeability either by the quasi-analytical solution (left curve) or by its own value obtained at $Re = 0$ (right curve). When rescaled by its own permeability k_S, the bounce-back results approach those obtained with the boundary interpolations. This comparison shows that most of the bounce-back error is coming from the 5% error in the Stokes regime.

For the values of $\tau \in [0.53, 0.56]$ used here, the global measurements obtained with the linear interpolations and multi-reflections in non-linear regimes are rather close together. They are also very close to the Ghaddar's solution. Unfortunately, we have not yet found another reference to compare with more accurately for non-linear flows.

Multi-reflection provides in a regular manner higher Re numbers than the linear interpolations. Similarly, bounce-back solution usually gives an under-estimated Re numbers. This is probably related to the fact that the effective radius (square fraction) obtained with bounce-back is higher than

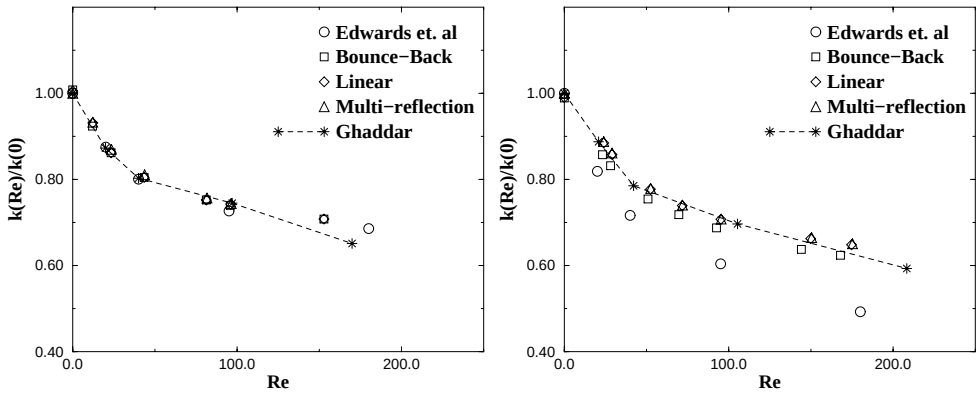

Figure 7: Dimensionless permeability values versus Re number at $c = 0.3$ (left) and $c = 0.5$ (right). In both cases, the quasi-analytical solution [33] in Stokes regime is used to rescale the apparent permeability.

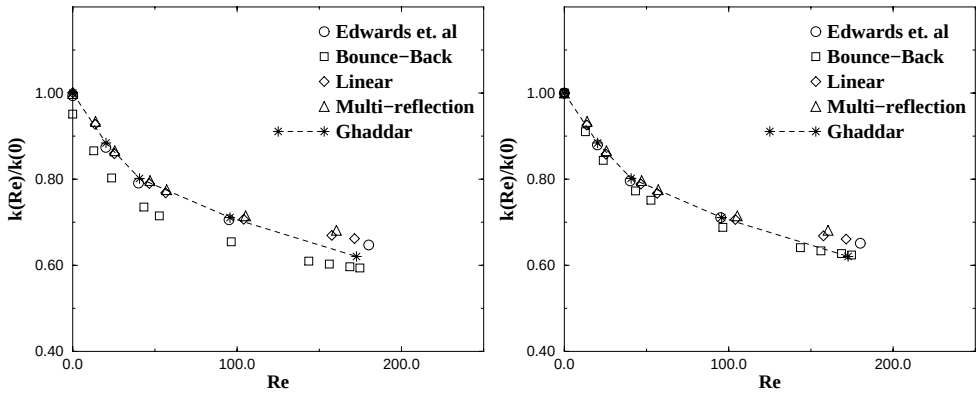

Figure 8: Dimensionless permeability values versus Re number for $c = 0.4$. Left: the permeability is scaled by the quasi-analytical solution [33] in Stokes regime. Right: the permeability for each method is scaled by its own value in the Stokes regime.

the expected value. We want also to stress that multi-reflections with the coefficients (56) converges much faster to stationary state than the solution (51). Whereas in the previous tests there were no total mass violation due

to the symmetry, in current tests we observe some loss of mass with respect to the initial distribution. For instance, the relative mass loss per time step at stationary regime for $c = 0.5$, $Re \approx 23$ is 4×10^{-7} by linear interpolation and 2.3×10^{-7} by multi-reflection. At $Re \approx 174$, these values are 4.7×10^{-6} and 6×10^{-7}. These data show that the mass violation increases with Re but its absolute values and rates are smaller for the multi-reflections. Similar results are obtained in other tests.

Table 17 in appendix D gives the dimensionless apparent permeability $\bar{k} = k/k_S$ values (right columns) versus Re numbers (left columns) for the linear interpolations.

6 Moving boundaries

6.1 Algorithms

6.1.1 Definitions

In order to test the robustness of the linear interpolations (24), (25) and multi-reflections (51), (56) in situations where the distance δ_q varies in a natural way, we construct moving boundary algorithms based on these boundary conditions.

The fluid points are defined as in section 3.1 and the other points are called *"solid"*. It is then natural to divide the corresponding solids into *"static"* and *"moving"* ones, depending upon the time behavior of their limiting surfaces: a solid is said *"static"* if its limiting surface does not change its position on the lattice, and *"moving"* otherwise. The points in static and moving solids are respectively called *static* and *moving solid points*. Accordingly, **at each time step** t, the boundary (fluid) points, defined as in section 3.1, are also divided into *"static"* and *"moving"* boundary points. The ones which *currently* have neighbors only in static solids are called *static boundary points* and are handled as described in section 3. The boundary points which have at least one neighbor in a moving solid, at link distance δ_q ($0 \leq \delta_q < 1$), are called *moving boundary points* and their treatment is described in the next sections. Fluid, moving solid, and boundary points of both kinds can exchange their status. The only restriction here is on the velocity of the solid body which must be less than 1 l.u. per time step in any direction so that the fluid/solid points cannot exchange their status without staying at least one time step in the boundary sets.

Note that in our computer implementation the static solid points are actually not stored (allocated), while we have found simpler to store the moving ones in all the following algorithms.

6.1.2 Connections to other methods

Starting from any time t our main algorithm go through the following substeps to get the new state at time $t+1$: collision, propagation, boundary conditions, analysis, advection of the moving solids, and reconstruction of new fluid points. The first four steps are identical to the ones used in section 5. The solid advection corresponds to a sampling of the position of the moving solids at a time $t^{ad.} = t + \Delta_t^{ad.}$, with $0 \leq \Delta_t^{ad.} \leq 1$. As a result of this advection step some fluid points become solid and some solid points become fluid. The state of these new boundary (fluid) points has to be supplied and in the available literature this is done along two main lines.

Along the first one (see for instance [40, 34]), called the *LB in fluid* technique in the sequel, the LB equation (1) and (2) is applied only in fluid points. The difficulty of this approach is that all the populations in the new boundary points have to be reconstructed. In [40], the equilibrium distribution with the mean density of the surrounding fluid and the velocity of the solid body is used. In [34], all the populations are interpolated from bulk with second order schemes. In our implementation we try to stay as close as possible to the static LB algorithm. We first obtain all possible populations by the advection step (1). Then the links opposite to the new cut ones are reconstructed using relation (21) with some necessary interpolations discussed in the next section. Finally, the remaining populations, called "tangential" below, are reconstructed explicitly (second part of the next section).

Along the second line (see for instance [23, 41]), called *LB in solid* in the sequel, the collision and propagation steps are applied in all the fluid and moving solid points (though the populations are recomputed as an equilibrium in [41]) and the state of the new fluid points is automatically supplied by the value they had in the solid. In addition the boundary conditions are applied on both (concave and convex) sides of the solid boundary in [23, 41]. In our *LB in solid* implementation the collision and propagation steps are applied unchanged everywhere. In particular the propagation takes place from fluid points to the solid ones according to the evolution equation (1) which, in our opinion, supplies the continuation of the solution from the fluid to the solid. When a solid point becomes a boundary fluid point, its populations

along the links from fluid to solid are already obtained from the advection step and the opposite cut links are reconstructed exactly as in our *LB in fluid* algorithm above (we have noticed that using the value they had in the solid leads to larger fluctuations of the solution). The other (tangential) links are the only ones actually keeping their value from the solid.

We compute the force according to (57) or (65) during the analysis step, before the points change theirs status from solid to fluid. This has to be contrasted with the computation of the force contribution from new fluid/solid points described in [40, 41]. Note also that in both our moving methods, the boundary conditions are applied only in the boundary fluid nodes.

Finally in the examples given in section 6.2, the dynamic of the solid objects does not depend on the computed forces, *i.e.* their velocity is prescribed. Further tests are required to evaluate our moving algorithms (especially the *LB in solid* one) when the solid dynamics depends on fluid solution.

6.1.3 Details of the moving schemes

Common to the *LB in fluid* and *LB in solid* algorithms.

The key point of our moving algorithm is the distinction between the "tangential" and "non-tangential" links in the new fluid points. A link q belongs to the set of tangential links $\mathcal{T}(\vec{r}_{\rm b})$, if $\vec{r}_{\rm b}-\vec{c}_q$ is also a new boundary fluid point or when both neighbors, $\vec{r}_{\rm b}+\vec{c}_{\bar{q}}$ and $\vec{r}_{\rm b}+\vec{c}_q$, are solid (*i.e.* $\vec{r}_{\rm b}$ is in a corner or a narrow channel). Note that $\mathcal{T}(\vec{r}_{\rm b})$ always contains the zero velocity $\vec{c_0}$. Otherwise, the link is a "non-tangential" link and belongs to the set $\overline{\mathcal{T}}(\vec{r}_{\rm b})$ (with $\mathcal{C}(\vec{r}_{\rm b})\subset\overline{\mathcal{T}}(\vec{r}_{\rm b})$).

The treatment of the "non-tangential" links is exactly the same for the *LB in fluid* and *LB in solid* algorithms. When $\vec{r}_{\rm b}-\vec{c}_q$ is a fluid point, we set $f_q(\vec{r}_{\rm b},t+1)$ according to the propagation step (1):

$$f_q(\vec{r}_{\rm b},t+1)=\tilde{f}_q(\vec{r}_{\rm b}-\vec{c}_q,t)\ . \tag{81}$$

When $\vec{r}_{\rm b}+\vec{c}_q$ belongs to a solid, we set $f_{\bar{q}}(\vec{r}_{\rm b},t+1)$ according to the boundary rules. However, since the post-collision population $\tilde{f}_q(\vec{r}_{\rm b},t)$ is not known at the new fluid point, one cannot use directly the bounce-back, upwind linear interpolation or multi-reflection boundary conditions. For the multi-reflection cases, one could bring the interpolation coefficient κ_1 to zero with the help of transformations (48) without loss of formal accuracy. However the resulting coefficients are not always found in "stability interval" $[-1;1]$.

In order to keep similar algorithms for all the boundary techniques under consideration, we interpolate $\tilde{f}_q(\vec{r}_{\rm b}, t+1)$ from the bulk. For multi-reflections, we have also to interpolate the second order post-collision term $\lambda_2 \tilde{f}_q^{(2)}$ (see (46)). The low order interpolations

$$\begin{aligned} \tilde{f}_q(\vec{r}_{\rm b}, t) &\approx 2\tilde{f}_q(\vec{r}_{\rm b} + \vec{c}_{\bar{q}}, t) - f_q(\vec{r}_{\rm b} + \vec{c}_{\bar{q}}, t) + O(\epsilon^2) \ , \\ \tilde{f}_q^{(2)}(\vec{r}_{\rm b}, t) &\approx \tilde{f}_q^{(2)}(\vec{r}_{\rm b} + \vec{c}_{\bar{q}}, t) + O(\epsilon^3) \ , \end{aligned} \tag{82}$$

are used to keep a minimal number of the communications between the neighboring points. In a similar way, we set $\tilde{\rho}$ in relations (6) and (20) equal to the arithmetical mean value $\bar{\rho}$, computed from the neighbor values $\rho(\vec{r}_{\rm b} + \vec{c}_{\bar{q}})$, $\bar{q} \notin \mathcal{C}(\vec{r}_{\rm b}) \cup \mathcal{T}(\vec{r}_{\rm b})$. Then the relations (24), (25) and multi-reflections (51), (56) can be used to compute the populations $f_{\bar{q}}(\vec{r}_{\rm b})$ according to relation (22).

Differences between the *LB in fluid* **and** *LB in solid* **algorithms**.

The only difference between our two algorithms is the treatment of the "tangential" links. In the *LB in solid* algorithm, the tangential populations keep the values they have obtained in the solid. In the *LB in fluid* algorithm they are computed assuming all the tangential links at equilibrium. Our heuristic assumes an incompressible flow for which the first (26) and second (27) order corrections of f_0 are equal to zero. In a similar way, the projection of the momentum derivatives (*i.e.* first and second order corrections) on the other tangential links can be neglected, otherwise the connected points would not appear from the solid at the same time.

In order to compute the equilibrium in the new fluid points, one has to estimate $\vec{\jmath}$ and ρ. A first-order approximation of the velocity $\vec{u}^{\rm ap\cdot}(\vec{r}_{\rm b}, t+1)$ is obtained from the arithmetical mean of the linear interpolations between the known values of the velocity $\vec{u}_{\rm w}(\vec{r}_{\rm b} + \delta_q \vec{c}_q, t)$ at the boundary and $\vec{u}(\vec{r}_{\rm b} - \vec{c}_q, t)$ for all $q \in \overline{\mathcal{T}}(\vec{r}_{\rm b})$ (the boundary velocity is used if $\overline{\mathcal{T}}(\vec{r}_{\rm b})$ is empty). Assuming then the equilibrium solution for the tangential links, the unknown density is derived from the linear equation:

$$\rho \left\{ 1 - \sum_{q \in \mathcal{T}} f_q^{eq\cdot}(1, \vec{u}^{\rm ap\cdot}) \right\} = \sum_{q \notin \mathcal{T}} f_q - \frac{1}{2} \sum_{q \in \mathcal{T}} t_p^\star \ \vec{c}_q \cdot \vec{F} \ , \tag{83}$$

We have found that relation (83) leads to slightly smaller oscillations in the solution than the direct use of the approximate density value at equilibrium. Noting that the values $\vec{u}(\vec{r}_{\rm b} - \vec{c}_q, t+1)$ in the "old" fluid points are already

known during the reconstruction of the tangential links, their values could be used instead of $\vec{u}(\vec{r}_{\rm b} - \vec{c}_q, t)$. However we have not detected any further improvement of the accuracy with this change.

6.2 Numerical results

6.2.1 Set-up for moving boundary tests.

In a first set-up we simulate a periodic flow past a cylinder (sphere) at rest, the velocity of flat (cylindrical) outer boundary being $-\vec{u}_{\rm w}$. We refer below to this set-up as to the *static solution* (shortly "s"). In static and linear regime, a cylinder between flat walls is considered in Section 5.1.6. The quasi-analytical Stokes solution for a sphere travelling along the cylinder axis is considered in [39]. Static LB solutions are compared with it in [18]. In the second set-up, an impulsively started cylinder (sphere) moves with velocity $\vec{u}_{\rm w}$ and the outer boundary is at rest. When the moving solid reaches the box boundaries, its position is adjusted by periodicity. We refer below to this set-up as to *moving solution* (or simply "m").

As in [34], we check for the Galilean invariance of the method by comparing the results of the first and second set-ups when the solids move with a constant velocity and the position of their center of mass $\vec{r}_c$ is given by

$$\vec{r}_c(t^{ad.}) = \vec{r}_c(\Delta_t^{ad.}) + \vec{u}_{\rm w} t \ , \qquad t \geq 0 \ . \tag{84}$$

If the flows are Galilean invariant we expect to obtain the velocity, pressure distributions and forces as

$$\vec{u}^{(\rm s)} = \vec{u}^{(\rm m)} - \vec{u}_{\rm w} \ , \quad P^{(\rm s)} = P^{(\rm m)} \ , \quad \vec{F}^{(\rm s)} = \vec{F}^{(\rm m)} \ , \tag{85}$$

where $P^{(\rm s)}$ and $P^{(\rm m)}$ are the pressure distributions minus some characteristic mean pressures. The forces are computed independently, once on the outer boundary and once on the inner solid, using the standard definition (57) or the force definition with boundary fitting (66). Since no external force is applied, the sum of the forces on the internal and external boundaries is expected to be zero for the stationary solutions. In order to check relations (85), we measure the values of the velocity and pressure when the moving solid is found at the same position as in the "s" case. We compare also the "m" forces and their averages during one period with their "s" counterparts. Here the period is defined as the minimal number time steps required to move

the solid to the same position, up to an integer displacement, with respect to the underlying lattice (assuming a rational value for $\vec{u}_{\rm w}$).

When the solid body moves, the LB solution is no longer stationary in the lattice frame. Since the unsteady Stokes equation does not possess Galilean invariance, we simulate the Navier-Stokes equation in "m" and "s" cases (even for small Re numbers). In the next sections our attention will be mostly focused on the *LB in fluid* algorithm and comparisons with the *LB in solid* one will be done for the multi-reflection case only.

6.2.2 Impulsively started cylinder in a channel

We consider a $1 \times 99 \times 201$ channel, periodic in the x- and z-directions. A cylinder, of radius $R = 12$ and axis along the x-direction, is moving along the z-axis with a velocity $u_{\rm w} = -0.04$. The cylinder starts at $t = 0$ from the point $(y, z) = (53.5, 29.65)$ and the time shift $\Delta_t^{ad.} = 0.5$.

	A	B	C	D
$E^{(2)}(\ p\ )$ [%]	2.16	0.81	2.4	5.31
$E^{(2)}(u_z)$ [%]	4.40	2.20	5.4	2.52
$E^{(2)}(u_y)$ [%]	1.81	0.05	0.16	0.05
Force at disk				
Static F_y	-0.024	-0.024	-0.024	-0.024
Static F_z	0.62	0.62	0.62	0.62
$E^{(\rm r)}(\bar{F}_y)$ [%]	5.7×10^{-3}	6×10^{-4}	1.6×10^{-2}	0
$E^{(\rm r)}(\bar{F}_z)$ [%]	0.34	0.26	0.37	0.26
$E^{(\rm r)}(F_y)$ [%]	4.5×10^{-3}	2.6×10^{-3}	3×10^{-3}	2.6×10^{-3}
$E^{(\rm r)}(F_z)$ [%]	2.5	0.56	0.57	0.95
Force at flat				
$E^{(\rm r)}(\bar{F}_y)$ [%]	4.4×10^{-3}	7×10^{-4}	1.1×10^{-3}	0
$E^{(\rm r)}(\bar{F}_z)$ [%]	0.29	0.08	3.6×10^{-2}	0.09
mass loss per period	2.9×10^{-7}	1.4×10^{-8}	3.2×10^{-7}	2.8×10^{-7}

Table 13: Comparison for a $1 \times 99 \times 201$-box, $\tau = 0.875$, of linear interpolations (A), multi-reflections (B), multi-reflections without correction (C), multi-reflections for the *LB in solid* algorithm (D).

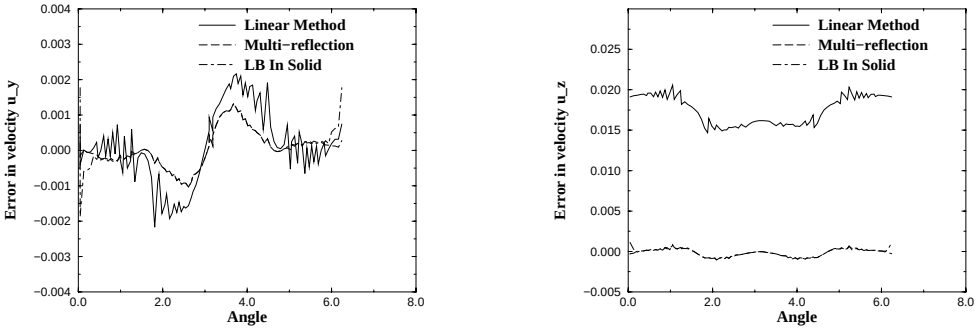

Figure 9: Relative difference between the moving and static velocities at the boundary points for a $1 \times 99 \times 201$ box and $\tau = 0.875$. "Linear Method" and "Multi-reflection" correspond to linear interpolations and multi-reflections for the *LB in fluid* method; "LB in Solid" corresponds to multi-reflection for the *LB in solid* method.

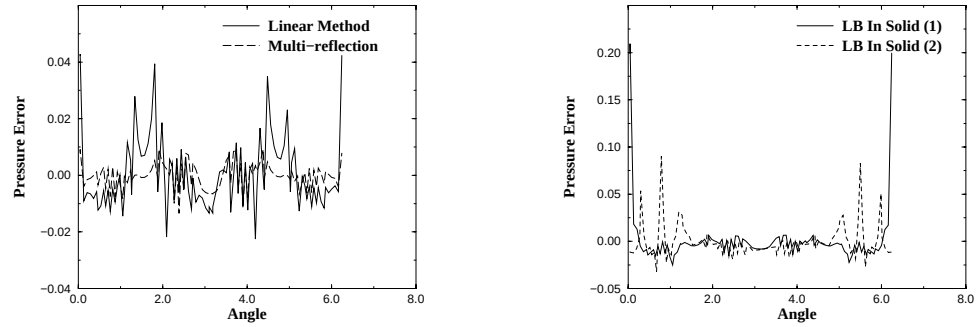

Figure 10: Relative pressure error corresponding to figure 9.

Case $Re = 7$

A stationary "static" solution is obtained for $\tau = 0.875$. The corresponding "moving" solution is compared with the static one at $t = 150743$ in point $(y_c, z_c) = (53.5, 29.99)$, when the cylinder finishes its 30st trip through the channel. Table 13 shows the relative error estimations (77) between static and moving solutions for pressure and velocity. Figures 9 and 10 show velocity and pressure error distributions at boundary points around the cylinder. Linear interpolations lead to larger difference between "s" and "m" solutions. In case of multi-reflection, the algorithms with and without

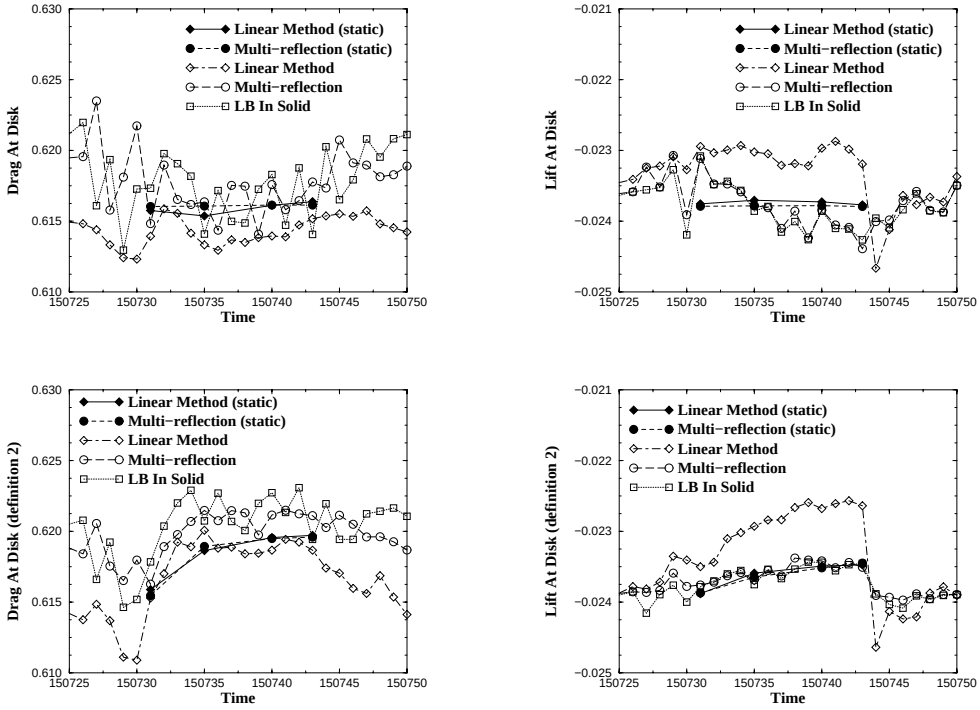

Figure 11: Drag and lift forces at disk, computed from (57), upper row, and (66), lower row, are plotted during one period.

internal fluid give very close results except for the points which have just changed their status from solid to liquid. For the *LB in solid* algorithm and $(y_c, z_c) = (53.5, 29.99)$, such points happen at the rear of the cylinder. The pressure in these points differs strongly from the bulk value (see Fig. 10, LB In Solid (1)) and contributes mainly to the pressure error. When no new point appears, the pressure fluctuations are twice smaller (see Fig. 10, LB In Solid (2)) and the corresponding $E^{(2)}(p)$ decreases from 5% to 3%. The comparison of the columns B and D in Table 13 confirms that the reconstruction of the tangential populations leads to smoother bulk solutions than its "in solid" counterpart.

Table 13 shows also the values of the forces in the static regime, the force on the flat wall being exactly the opposite of the force on the disk. The relative differences (76) between the static and moving forces ($E^{(\mathrm{r})}(F_y)$ and $E^{(\mathrm{r})}(F_z)$) and the difference between the "s" force at (y_c, z_c) and the "m"

	A	B	C	D
Force at disk				
Static F_y	1.21×10^{-4}	0.281	0.279	0.281
Static F_z	0.86	0.797	0.797	0.797
$E^{(\mathrm{r})}(F_y)$ [%]	1.62×10^{-2}	1.1×10^{-2}	3.1×10^{-2}	1.0
$E^{(\mathrm{r})}(F_z)$ [%]	3.6	3.78	15	4.77
Force at flat				
Static F_y	3.27×10^{-3}	-0.279	-0.281	-0.278
Static F_z	-0.91	-0.911	-0.911	-0.911
$E^{(\mathrm{r})}(F_y)$ [%]	4.1×10^{-3}	6.7×10^{-2}	0.08	6.7×10^{-2}
$E^{(\mathrm{r})}(F_z)$ [%]	0.21	0.24	0.29	0.24
mass loss per period	2.9×10^{-7}	1.9×10^{-7}	5.2×10^{-7}	1.6×10^{-7}

Table 14: Same as Table 13 for $\tau = 0.5144$.

force averaged over one period (here 25 time steps) ($E^{(\mathrm{r})}(\bar{F}_y)$ and $E^{(\mathrm{r})}(\bar{F}_z)$) are also given. This last comparison is justified if the force changes weakly in the static regime compared with the moving one when the cylinder center shifts within one lattice unit. This is the case here as demonstrated in Figure 11 where the lift and drag distributions during one period are shown for the moving case (for comparison the static solution is also given for some cylinder positions). The upper and lower rows correspond respectively to the force definitions (57) and (66). In the static case, as for the Stokes results of section 5.1.5, the force (57) fluctuation are bigger for the linear interpolations than for the multi-reflections. In the moving case, the oscillations of both methods are similar for the drag. For the lift, they are stronger for the linear interpolations than with the multi-reflections. Also, whereas the multi-reflection solution fluctuates around its corresponding static value, the linear interpolation solution deviates from it.

Case $Re = 200$

When $\tau = 0.5144$, the solution is no longer stationary. It appears an almost periodic-doubling pattern for the drag (probably due to the fact that the cylinder axis is slightly off the middle of the two flat walls) and an almost periodic one for the lift (it is difficult to be more precise since the final regime has not yet been reached at the end of the simulations). The left column in

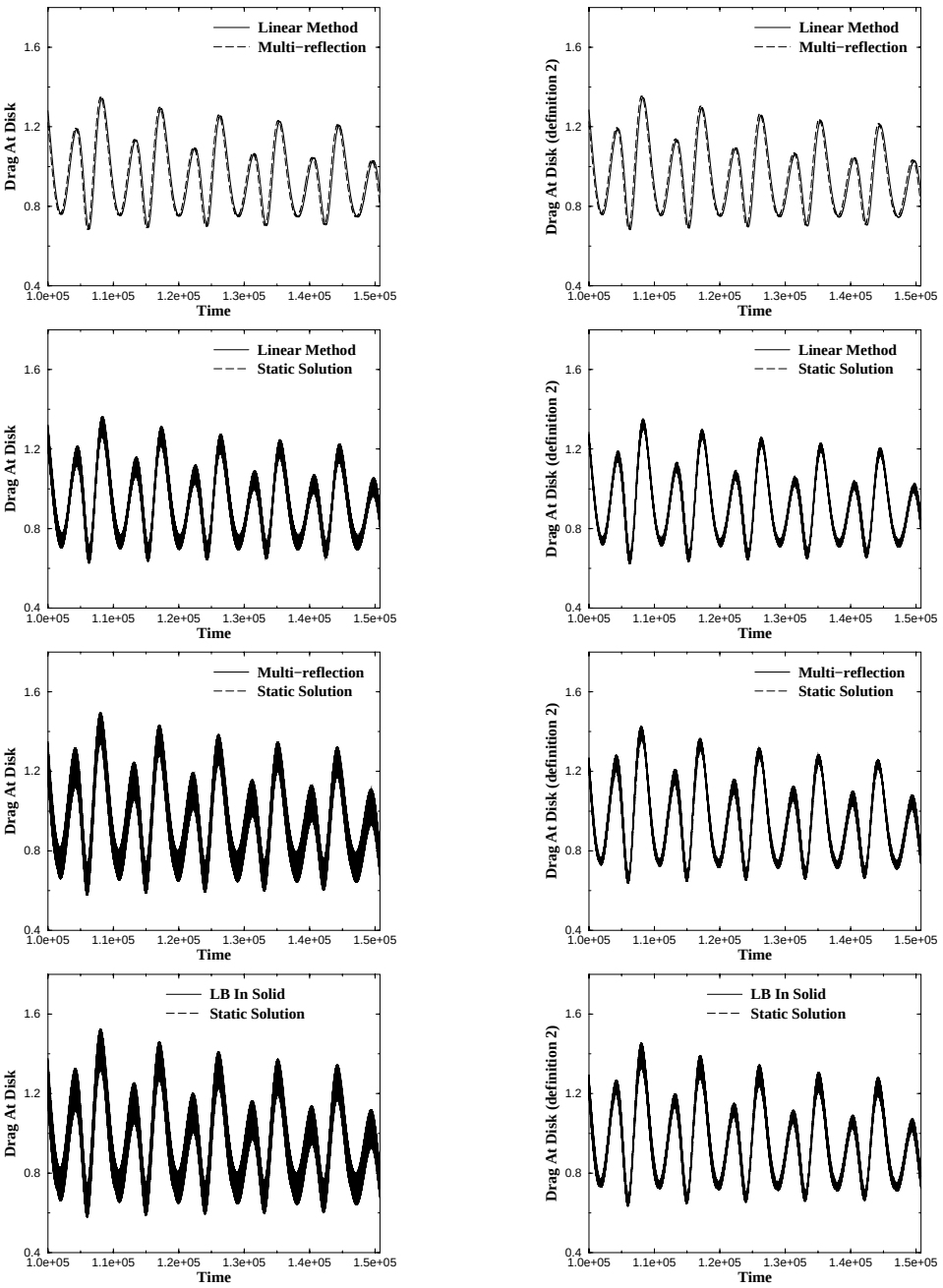

Figure 12: Drag on the cylinder as a function of time; from top to bottom: "static", linear reflection, *LB in fluid* and *LB in solid* multi-reflection algorithms; the force is computed with definitions (57), left, and (66), right.

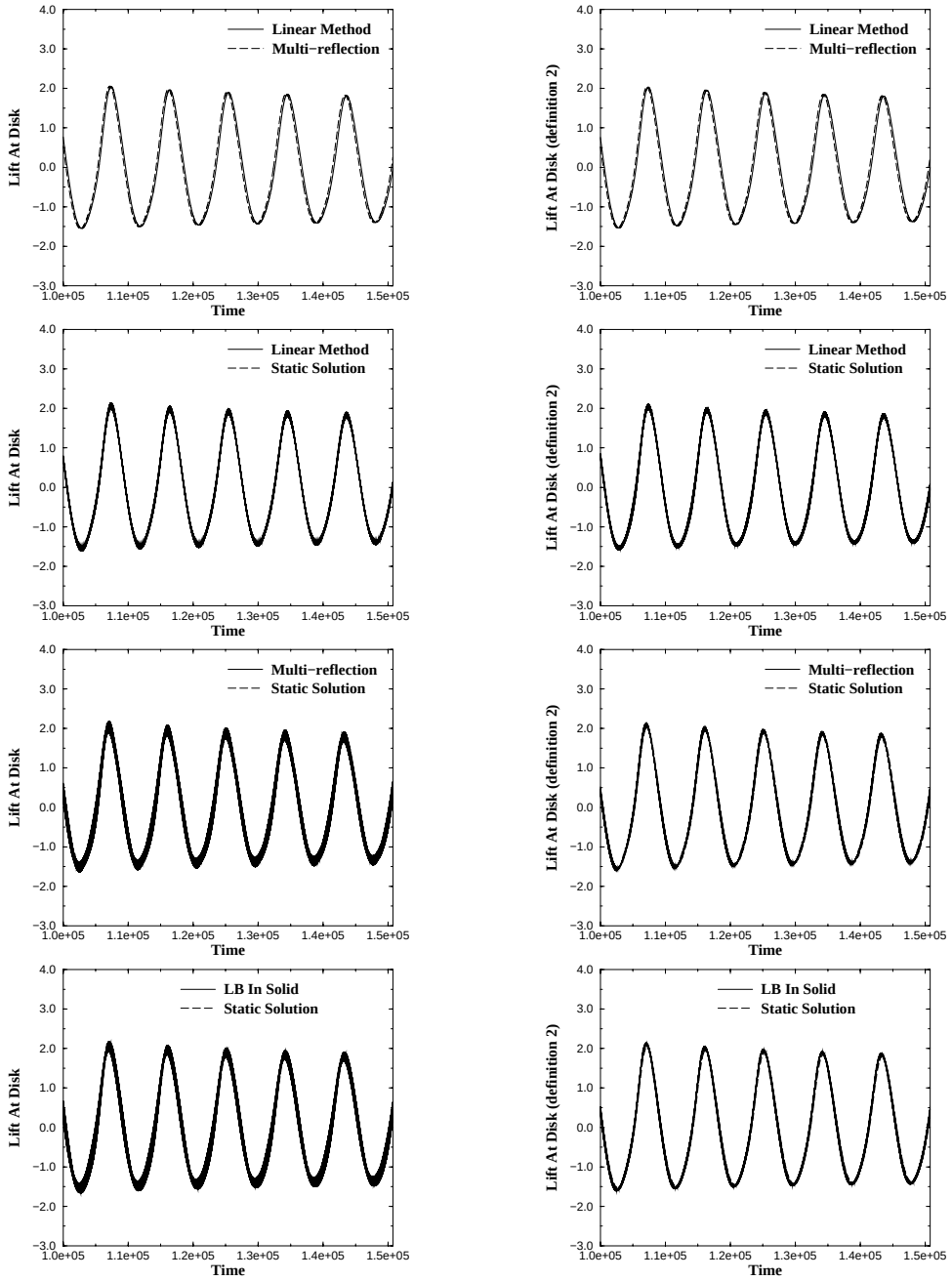

Figure 13: Lift on the cylinder as a function of time; from top to bottom: "static", linear reflection, *LB in fluid* and *LB in solid* multi-reflection algorithms; the force is computed with definitions (57), left, and (66), right.

figures 12 and 13 shows drag and lift forces as functions of time computed with the definition (57) at cylinder boundary and the right one shows the same quantities but computed with the definition (66). Since the flat walls are located at a distance equal to 0.5 of the nearest lattice nodes, both force definitions coincide for the flat wall. The results are plotted for the static case and three moving techniques: linear interpolations and multi-reflections for the *LB in fluid* and *LB in solid* algorithms. The error estimations are also given in Table 14. Since the solution is nonstationary, the comparison is only done, without averaging, when the cylinder is at the same location for the static and moving cases.

Some remarks are now in order for $Re = 200$. First, when the forces are computed in the standard way, the multi-reflection *LB in solid* algorithm is found to be the most "oscillatory" one, followed by the *LB in fluid* algorithm, the linear interpolation algorithm giving the "smoothest" results. When the force distribution with boundary fitting (66) is used, the smoothness of all solutions, and especially of the *LB in fluid* algorithm with multi-reflection, is improved drastically. One technical explanation could be that the force computation (66) involves populations from the next to boundary nodes where the solution fluctuates less. Also, when the surface integration error with (66) happens to be smaller than with definition (57), new definition improves the computation of forces since the stress values are approximated on the surface. This is also consistent with the fact that the best filtering is achieved for the multi-reflection algorithms, which have been designed to be the most accurate near the boundaries.

6.2.3 Moving sphere in a cylinder

We consider a sphere of radius $R_s = 16.9$ in a periodic motion along the x-axis of an outer cylinder of radius $R_c = 42.5$ and length $\ell = 189$ along x (in l.u.). The sphere starts from the point $(x_0, y_0, z_0) = (30.65, 4.225, 0)$, with respect to the cylinder axis, and moves with velocity $u_{\mathrm{w}} = -0.04$. The moving solution is compared with the static one after 31 cycles across the cylinder. Quasi-stationary solutions are reached in the "m" and "s" regimes. The results for forces are shown in Table 15. The drag and lift values are rescaled by the viscous scaling $\vec{M}^{(\mathrm{t})}/(6\pi\mu\|\vec{u}_{\mathrm{w}}\|R\,k^{\star})$, where $k^{\star}$ is a function of the ratio between the sphere and cylinder radii given in [34, 39]. The table shows that in this test the errors on the force are about twice smaller for the multi-reflection algorithm than for the linear interpolation one.

	Linear	Multi-reflection
Force at sphere		
Static F_x	0.683	0.688
Static F_y	-3.02×10^{-3}	-3.02×10^{-3}
$E^{(\mathrm{r})}(\bar{F}_x)$ [%]	2.48	1.63
$E^{(\mathrm{r})}(\bar{F}_y)$ [%]	1.7×10^{-3}	0.7×10^{-3}
$E^{(\mathrm{r})}(F_x)$ [%](at sphere)	1.2	0.56
$E^{(\mathrm{r})}(F_y)$ [%](at sphere)	4.0×10^{-3}	2.3×10^{-3}
Force at cylinder		
Static F_x	-0.682	-0.689
Static F_y	3.02×10^{3}	3.02×10^{3}
$E^{(\mathrm{r})}(\bar{F}_x)$ [%]	2.79	0.54
$E^{(\mathrm{r})}(\bar{F}_y)$ [%]	8×10^{-4}	3×10^{-4}
mass loss per period	3.2×10^{-6}	1.8×10^{-6}

Table 15: Comparison between the static and moving solution for a sphere in a cylinder at $\tau = 0.55$ using the linear interpolation and multi-reflections *LB in fluid* algorithms.

7 Conclusion

We have shown that boundary conditions based on a link approach such as [14] can be analyzed in the spirit of [2, 3, 4, 10] and their accuracy can be assessed for simple flows such as Couette or Poiseuille-Hagen ones. From this analysis we have been able to derive new boundary conditions for which a formal third-order accuracy can be proven theoretically for steady linear or non-linear LB solutions, leading to the Stokes and Navier-Stokes equations.

These theoretical results have been confirmed by several simulations of flows in periodic arrays of spheres or cylinders in the Stokes regime and of cylinders for the Navier-Stokes one.

We would like to stress that the bounce-back condition has still several advantages: it is simple, robust and obeys a strict mass conservation. This is especially true for simulations in complex geometries such as those coming from weakly resolved tomography in which the boundary position is only approximately known. In addition the bounce-back accuracy can be very satisfactory if the following rules are obeyed. First the no-slip condition has

to be set in the middle of the cut links. Secondly the eigenvalues of the collision matrix for the odd and even moments must be chosen such that the corresponding Λ^2 in (40) is set to a constant value between 1/6 and 1/4: fixed Λ^2 ensures viscosity independent measurements.

We have shown that the linear interpolation improves the overall accuracy over the bounce-back condition for low viscosities and curved walls. The multi-reflection method provides a further improvement in accuracy for any combination of the collision eigenvalues, especially for the hydrodynamics quantities near the walls.

The present theoretical analysis, done for steady flows, has to be extended to the unsteady situations. Two theoretical difficulties have also to be studied in more details: it would be useful to go beyond the heuristic arguments used here to deal with the stability issue; it would also be interesting to find a way to keep the accuracy of the multi-reflection without any mass loss.

Finally, the method has been extended to moving boundaries. Although we have only done a preliminary study, interpolations and multi-reflections exhibit a good overall stability even in changing geometries. As seen by other authors, we confirm that the main difficulty of these simulations comes from an unreliable reconstruction of the pressure in the new fluid points, leading to numerical fluctuations of the physical quantities.

Acknowledgments

We would like to thank K. Steiner, P. Lallemand and L.-S. Luo for stimulating discussions. Special thanks are given to P. Klein and M. Beck for numerical help. This work was supported by DFG Project "Die verallgemeinerte Lattice Boltzmann Methode für freie Randwertprobleme und Mehrphasenströmungen". DH also thanks ITWM for its hospitality during this work.

A Taylor expansion for boundary conditions

In this section we are giving the Taylor expansion for steady solutions of the LB equation. To shorten the formulae the time dependencies are omitted and the right-hand sides are taken at $\vec{r}_{\mathrm{b}}$. Note also that the second-order derivatives of P and of the non-linear terms are neglected since they appear

at the same order as the third-order derivatives of the momentum.

$$
\begin{aligned}
f_{\bar{q}}(\vec{r}_{\rm b}) &= t_p^\star \left(P - j_q - I_{\rm f} F_q + \frac{3j_q^2 - j^2}{2\tilde{\rho}} \right) \\
&+ f_q^{(1)} - f_q^{(2)} \ , \qquad \text{(A.1)} \\
\tilde{f}_q(\vec{r}_{\rm b}) &= t_p^\star \left(P + j_q + I_{\rm f} F_q + \frac{3j_q^2 - j^2}{2\tilde{\rho}} + F_q \right) \\
&+ (1-\lambda_\nu) f_q^{(1)} + (1-\lambda_2) f_q^{(2)} \ , \qquad \text{(A.2)} \\
\tilde{f}_q(\vec{r}_{\rm b} - \vec{c}_q) &= t_p^\star \left(P + j_q + I_{\rm f} F_q + \frac{3j_q^2 - j^2}{2\tilde{\rho}} + F_q \right) \\
&+ (1-\lambda_\nu) f_q^{(1)} + (1-\lambda_2) f_q^{(2)} \\
&- t_p^\star \left(\partial_q P + \partial_q j_q + \partial_q \left(\frac{3j_q^2 - j^2}{2\tilde{\rho}} \right) \right) \\
&+ \frac{1}{2} t_p^\star \partial_{qq} j_q - (1-\lambda_\nu) \partial_q f_q^{(1)} \ , \qquad \text{(A.3)} \\
\tilde{f}_q(\vec{r}_{\rm b} - 2\vec{c}_q) &= t_p^\star \left(P + j_q + I_{\rm f} F_q + \frac{3j_q^2 - j^2}{2\tilde{\rho}} + F_q \right) \\
&+ (1-\lambda_\nu) f_q^{(1)} + (1-\lambda_2) f_q^{(2)} \\
&- 2t_p^\star \left(\partial_q P + \partial_q j_q + \partial_q \left(\frac{3j_q^2 - j^2}{2\tilde{\rho}} \right) \right) \\
&+ 2t_p^\star \partial_{qq} j_q - 2(1-\lambda_\nu) \partial_q f_q^{(1)} \ , \qquad \text{(A.4)} \\
\tilde{f}_{\bar{q}}(\vec{r}_{\rm b}) &= t_p^\star \left(P - j_q - I_{\rm f} F_q + \frac{3j_q^2 - j^2}{2\tilde{\rho}} - F_q \right) \\
&+ (1-\lambda_\nu) f_q^{(1)} - (1-\lambda_2) f_q^{(2)} \ , \qquad \text{(A.5)} \\
\tilde{f}_{\bar{q}}(\vec{r}_{\rm b} - \vec{c}_q) &= t_p^\star \left(P - j_q - I_{\rm f} F_q + \frac{3j_q^2 - j^2}{2\tilde{\rho}} - F_q \right) \\
&+ (1-\lambda_\nu) f_q^{(1)} - (1-\lambda_2) f_q^{(2)} \\
&- t_p^\star \left(\partial_q P - \partial_q j_q + \partial_q \left(\frac{3j_q^2 - j^2}{2\tilde{\rho}} \right) \right) \\
&- \frac{1}{2} t_p^\star \partial_{qq} j_q - (1-\lambda_\nu) \partial_q f_q^{(1)} \ . \qquad \text{(A.6)}
\end{aligned}
$$

B Examples of momentum transport.

B.1 Non-inclined channel

When the force addition in each cell is independent on the position of the boundary (*i.e.* effective volume of the cell), the momentum transport definition (57) is independent on the actual boundary position (see relation (65)). Consequently, even if the population $f_{\bar{q}}$ is constructed to better fit the boundary, the force $\vec{M}^{(c)}$ will stay the same as for the bounce-back reflection.

Let us illustrate this by the simple example of Poiseuille flow in a channel of width H. If the momentum transport is calculated with definition (57), k is equal to $\nu Q/(FH^l)$, where H^l is number of liquid points across the channel. Even if the exact value $F\,H^3/(12\nu)$ of the flow rate Q is used, the measured permeability is equal to its exact value $H^2/12$ only if $H = H^l$, whereas the result is always exact with definition (66).

B.2 Example: Inclined channel

We consider either a Couette flow,

$$\frac{\partial^2 j_{x'}}{\partial z'^2} = 0, \quad j_{x'}(h') = 1, \quad j_{x'}(-h') = 0\ , \quad \rho \equiv \rho_0, \quad \nabla P \equiv 0\ , \tag{B.7}$$

or a Poiseuille flow

$$-F_{x'} = \nu \frac{\partial^2 j_{x'}}{\partial z'^2}, \quad j_{x'}(\pm h') = 0, \quad \rho \equiv \rho_0, \quad \nabla P \equiv 0\ , \tag{B.8}$$

in an inclined channel of width $2h'$, where the coordinates are written in a system rotated to align the x'-axis with the flow as

$$\begin{aligned} x' &= x\,\cos\theta + z\,\sin\theta\ , & z' &= -x\sin\theta + z\cos\theta\ , \\ x &= x'\cos\theta - z'\sin\theta\ , & z\ &= x'\sin\theta + z'\cos\theta\ . \end{aligned} \tag{B.9}$$

The exact linear solution is given, for Couette flow, by

$$N_i(\vec{r}) = t_p^\star \left\{ c_s^2\rho_0 + j_{x'}c_{ix'} + \frac{1}{\lambda_\nu}\frac{\partial j_{x'}}{\partial z'} c_{ix'}c_{iz'} \right\}, \qquad i = 0, \ldots, b_m. \tag{B.10}$$

and, for Poiseuille flow, by

$$N_i(\vec{r}) = t_p^\star \left\{ c_s^2\rho_0 + (j_{x'} + I_{\rm f}F_{x'})c_{ix'} + \frac{1}{\lambda_\nu}\frac{\partial j_{x'}}{\partial z'}c_{ix'}c_{iz'} - \frac{\nu}{\lambda_2}\frac{\partial^2 j_{x'}}{\partial z'^2}c_{ix'}(1-3c_{iz'}^2)\right\}, \qquad i=0,\ldots,b_m. \quad \text{(B.11)}$$

The substitution of (B.10) and (B.11) into (66) and (67), with the help of relation (68), yields at $z' = \pm h'$ the exact result

$$\vec{M}^{(\rm n)}(\pm h') = \sum_{q\in\mathcal{C}(\pm h')} t_p^\star \left\{ 2c_s^2\rho_0 - 6\nu \left.\frac{\partial j_{x'}}{\partial z'}\right|_{\pm h'} c_{qx'}c_{qz'}\right\}\vec{c}_q \ , \qquad \text{(B.12)}$$

with

$$\nu\frac{\partial j_{x'}}{\partial z'} = \frac{\nu}{2h'} \ , \qquad \text{for Couette flow} \ , \qquad \text{(B.13)}$$

$$\nu \left.\frac{\partial j_{x'}}{\partial z'}\right|_{\pm h'} = \mp F_{x'}h' \ , \qquad \text{for Poiseuille flow} \ . \qquad \text{(B.14)}$$

For Couette flow, relation (B.12) reads

$$\vec{M}^{(\rm n)}(\pm h') = A_{\rm S}\left(c_s^2\rho_0\vec{n}_\pm \pm \frac{\nu}{2h'}\vec{i}_s\right), \qquad \text{(B.15)}$$

where $\vec{n}_\pm$ are the normal vectors at $z' = \pm h'$ as defined in section 4 and $\vec{i}_s$ is the unit vector along the flow. For Poiseuille flow, relation (B.12) reads

$$\vec{M}^{(\rm n)}(\pm h') = A_{\rm S}(c_s^2\rho_0\vec{n}_\pm + F_{x'}h'\vec{i}_s) \ , \qquad \text{(B.16)}$$

then the total momentum transport, $\vec{M}^{(\rm n)} = \vec{M}^{(\rm n)}(-h') + \vec{M}^{(\rm n)}(h') = V^{\rm ef.}F_{x'}$, is equal to the force applied in the *effective volume* $V^{\rm ef.} = 2h'A_{\rm S}$, whereas it is in the volume V^l, independent of the boundary conditions, when using definition (57).

B.3 Example: Circular pipe

The solution of the Poisson equation in a circular pipe of radius R is

$$j_y = -\frac{F_y}{4\nu}(r^2 - R^2) \ , \quad r^2 = x^2 + z^2 \ , \quad 0 \le r \le R \ . \qquad \text{(B.17)}$$

For this flow the second order expansion gives also an exact solution similar to (B.11) and relation (66) is also exact.

Since the value of $\nu\partial_r j_y$ at $r = R$ is $-R\,F_y/2$, definition (66) yields

$$\vec{M}^{(\mathrm{n})} \approx \frac{R\,F_y}{2} \times 2\pi R\,\ell\,\vec{i}_y \;, \tag{B.18}$$

where ℓ is the length of the cylinder along the y-axis. Then the accuracy with the new definition depends of the evaluation of the surface integral $2\pi R\,\ell$ in (B.18). Whereas for definition (57), relation (65) reads

$$\vec{M}^{(\mathrm{c})} = F_y V^l \vec{i}_y \;, \tag{B.19}$$

and the precision of the total force computation depends on the accuracy of the discretization of a circle on lattice cells: $V^l/\ell \approx \pi R^2$.

C Multi-pole solution for a flow past square array of cylinders between flat walls

A quasi-analytical solution is obtained from a modification of the multi-pole procedure [33] to capture Dirichlet conditions at the flat walls. The method is based on the computation of the stream function ψ as a truncated series of terms which are solution of

$$\Delta^2\psi = 0 \;, \tag{C.1}$$

and satisfy the no-slip condition on the cylinder and the symmetries with respect to its center. The coefficients are then obtained from a least-square fit of boundary conditions at $y = H$ and $z = H$. In [33] the boundary conditions are $\psi = 1$ and $\omega = 0$ on the plane $y = H$ and $\partial_z\psi = \partial_z\omega = 0$ on the plane $z = H$ in order to match the periodic conditions and a scaled seepage velocity. In our calculation the boundary conditions are $\partial_y\psi = -\vec{u}_{\mathrm{w}}$ and $\partial_z\psi = 0$ on $y = H$ and $P = 0$ and $\partial_z\psi = 0$ on $z = H$.

The only difficulty we have found was a severe loss of accuracy (around one digit per term) when summing the series. We have solved the problem by doing the calculation with the Mathematica software with an intermediate accuracy set to twice the number of terms in the sum. The solution for the drag F^d is normalized as in (80) and tabulated in Table 16 which contains also the seepage velocity value scaled by the wall velocity $\vec{u}_{\mathrm{w}}$.

c	$F^d/\mu u_{\mathrm{w}}$	$Q_z/\rho u_{\mathrm{w}}$
0.1	5.34388	0.384425
0.2	6.86103	0.297680
0.3	8.75675	0.232982
0.4	11.4558	0.177666
0.5	15.7519	0.127767
0.6	23.8738	0.0812631
0.7	45.9788	0.0368363

Table 16: Scaled drag and seepage velocity for a square array of cylinders between moving flat walls as functions of the volume fractions c.

D Relative permeability of a square array of cylinders

As reference values, we give in Table 17 the relative permeability obtained by the LMB method with the linear interpolation as described in section 5.2.

$c = 0.2$		$c = 0.3$		$c = 0.4$		$c = 0.5$		$c = 0.6$	
22.66	0.86	12.06	0.93	13.64	0.93	23.82	0.88	22.33	0.90
29.44	0.84	23.26	0.86	25.28	0.86	28.89	0.86	30.30	0.85
42.56	0.81	43.40	0.80	46.46	0.79	52.34	0.78	47.97	0.77
67.85	0.77	81.18	0.75	56.52	0.77	71.67	0.74	64.10	0.72
102.0	0.74	96.12	0.74	104.0	0.71	95.24	0.71	113.0	0.64
128.4	0.73	124.6	0.72	157.5	0.67	149.9	0.66	124.1	0.62
151.9	0.72	152.8	0.71	171.4	0.66	174.6	0.65	131.4	0.61

Table 17: Re numbers and the corresponding dimensionless apparent permeability $\bar{k} = k/k_S$ values for a 66^2 box; k_S corresponds to (80).

References

[1] C. Cercignani, in *The Boltzmann Equation and Its Applications* (Springer, 1988) pp. 252–260.

[2] R. Cornubert, D. d'Humières, and D. Levermore, A Knudsen layer theory for lattice gases, *Physica* **D47**, 241–259 (1991).

[3] I. Ginzbourg and P. M. Adler, Boundary flow condition analysis for three-dimensional lattice Boltzmann model, *J. Phys. II France* **4**, 191–214 (1994).

[4] I. Ginzbourg, Boundary conditions problems in lattice gas methods for single and multiple phases, (Ph.D. thesis, Université Pierre et Marie Curie, Paris 1994).

[5] D. P. Ziegler, "Boundary Conditions for Lattice Boltzmann Simulations", *J. Stat. Phys.* **71**, 1171–1177 (1993).

[6] P. A. Skordos, Initial and boundary conditions for the lattice Boltzmann method. *Phys. Rev.* E **48**, 4823–4842 (1993).

[7] D. R. Noble, S. Chen, J. G. Georgiadis, and R. O. Buckius, A consistent hydrodynamic boundary condition for the lattice Boltzmann method, *Phys. Fluids* A **7**, 203–209 (1995).

[8] D. R. Noble, J. G. Georgiadis, and R. O. Buckius, Direct assessment of lattice Boltzmann hydrodynamics and boundary conditions for recirculating flows, *J. Stat. Phys.* **81**, 17–33 (1995).

[9] T. Inamuro, M. Yoshino, and F. Ogino, A non-slip boundary condition for lattice Boltzmann simulations, *Phys. Fluids* **7** (12), 2928–2930 (1995).

[10] I. Ginzbourg and D. d'Humières, Local second-order boundary method for lattice Boltzmann models, *J. Stat. Phys.* **84** (5/6), 927–971 (1996).

[11] O. Filippova and D. Hänel, Boundary-fitting and local grid refinement for lattice-BGK models, *Int. J. Mod. Phys.* C **9**, 1271–1279 (1998).

[12] H. Chen, C. Teixeira, and K. Molvig, Realization of fluid boundary conditions via discrete Boltzmann dynamics, *Int. J. Mod. Phys.* C **9**, 1281–1292 (1998).

[13] R. Mei, L.-S. Luo, and W. Shyy, An Accurate Curved Boundary Treatment in the Lattice Boltzmann Method, *J. Comp. Phys.* **155**, 307–330 (1999).

[14] M. Bouzidi, M. Firdaouss, P. Lallemand, Momentum transfer of a Boltzmann-lattice fluid with boundaries, *Phys. Fluids* **13**, 3452–3459 (2001).

[15] R. Verberg and A. J. C. Ladd, Accuracy and stability of a lattice-Boltzmann model with subgrid scale boundary conditions, *Phys. Rev. E* **65**, 016701-1–16 (2001).

[16] D. d'Humières, Generalized lattice-Boltzmann equations. In *Rarefied Gas Dynamics: Theory and Simulations.* (eds. B. D. Shizgal and D. P. Weaver), Progress in Astronautics and Aeronautics **59**, pp. 450–548 (1992).

[17] P. Lallemand and L.-S. Luo, Theory of the lattice Boltzmann method: Dispersion, dissipation, isotropy, Galilean invariance, and stability, *Phys. Rev.* E **61**, 6546–6562 (2000).

[18] D. d'Humières, M. Bouzidi, and P. Lallemand, Thirteen-velocity three-dimensional lattice Boltzmann model, *Phys. Rev.* E **63**, 066702-1–7 (2001).

[19] D. d'Humières, I. Ginzburg, M. Krafczyk, P. Lallemand, and L.-S. Luo, Multiple-relaxation-time lattice Boltzmann models in three dimensions, *Phil. Trans. R. Soc. Lond. A* **360**, 437–451 (2002).

[20] U. Frisch, D. d'Humières, B. Hasslacher, P. Lallemand, Y. Pomeau, and J.P. Rivet, Lattice gas hydrodynamics in two and three dimensions, *Complex Sys.* **1**, 649–707 (1987).

[21] X. He and L.-S. Luo, Lattice Boltzmann model for the incompressible Navier-Stokes equation, *J. Stat. Phys.* **88** (3/4), 927–944 (1997).

[22] A. J. C. Ladd, Numerical simulations of particulate suspensions via a discretized Boltzmann equation. Part 1. Theoretical foundation, *J. Fluid Mech.* **271**, 285–309 (1994).

[23] A. J. C. Ladd, Numerical simulations of particulate suspensions via a discretized Boltzmann equation. Part 2. Numerical results, *J. Fluid Mech.* **271**, 311–339 (1994).

[24] J. M. Buick and C. A. Greated, Gravity in a lattice Boltzmann model, *Phys. Rev.* E **61**, 5307–5320 (2000).

[25] Y. Qian, D. d'Humières, P. Lallemand, Lattice BGK models for Navier-Stokes equation, *Europhys. Lett.* **17**, 479–484 (1992).

[26] H. Chen, S. Chen, and W. H. Matthaeus, Recovery of the Navier-Stokes equations using a lattice-gas Boltzmann method, *Phys. Rev. A* **45**, R5339–5342 (1992).

[27] L. Giraud, Fluides visco-élastique par la méthode de Boltzmann sur réseau, (Ph.D. thesis, Université Pierre et Marie Curie, Paris 1997).

[28] R. Cornubert, Conditions aux limites des modèles cinétiques discrets: Couche de Knudsen et obstacles, (Ph.D. thesis, Université Pierre et Marie Curie, Paris 1991).

[29] D. Reinel-Bitzer, Calculation of material parameters in porous media, (ITWM Annual Report, Kaiserslautern, 1998).

[30] H. Hasimoto, On the periodic fundamental solutions of the Stokes equations and their application to viscous flow past a cubic array of spheres, *J. Fluid. Mech.* **5**, 317–328 (1959).

[31] A. S. Sangani and A. Acrivos, Slow flow through a periodic array of spheres, *Int. Journal of Multiphase Flow* **8** (4), 343–360 (1982).

[32] P. Adler, *Porous Media: geometry and transports* (Butterworth/ Heinemann, 1992)

[33] A. S. Sangani and A. Acrivos, Slow flow past periodic arrays of cylinders with application to heat transfer, *Int. J. Multiphase Flow* **8** (3), 193–206 (1982).

[34] P. Lallemand and L.-S. Luo, Lattice Boltzmann Method for Moving Boundary Problem, preprint (2001).

[35] D. A. Edwards, M. Shapiro, P. Bar-Yoseph, and M. Shapira, The influence of Reynolds number upon the apparent permeability of spatially periodic arrays of cylinders, *Phys. Fluids A* **2** (1), 45–55 (1990).

[36] C. Ghaddar, On the permeability of unidirectional fibrous media: A parallel computational approach, *Phys. Fluids* **7** (11), 2563–2586 (1995).

[37] A. J. C. Ladd, Moderate Reynolds number flows through periodic and random arrays of aligned cylinders, *J. Fluid Mech.* **349**, 31–66 (1997).

[38] J. Happel and H. Brenner, *Low Reynolds Number Hydrodynamics* (Prentice-hall, Englewood Cliffs, New Jersey, 1965).

[39] M. Tözeren, Drag on eccentrically positioned spheres translating and rotating in tubes, *J. Fluid Mech.* **129**, 77-90 (1983).

[40] C. K. Aidun, Y. Lu, and E.-J. Ding, Direct analysis of particulate suspensions with inertia using the discrete Boltzmann equation, *J. Fluid Mech.* **373**, 287-311 (1998).

[41] M. W. Heemels, M. H. J. Hagen, and C. P. Lowe, Simulating Solid Colloidal Particles Using the Lattice-Boltzmann Method, *J. Comp. Phys.* **164**, 48–61 (2000).

Published reports of the Fraunhofer ITWM

The PDF-files of the following reports are available under:
www.itwm.fraunhofer.de/zentral/berichte.html

1. D. Hietel, K. Steiner, J. Struckmeier

A Finite - Volume Particle Method for Compressible Flows

We derive a new class of particle methods for conservation laws, which are based on numerical flux functions to model the interactions between moving particles. The derivation is similar to that of classical Finite-Volume methods; except that the fixed grid structure in the Finite-Volume method is substituted by so-called mass packets of particles. We give some numerical results on a shock wave solution for Burgers equation as well as the well-known one-dimensional shock tube problem.
(19 pages, 1998)

2. M. Feldmann, S. Seibold

Damage Diagnosis of Rotors: Application of Hilbert Transform and Multi-Hypothesis Testing

In this paper, a combined approach to damage diagnosis of rotors is proposed. The intention is to employ signal-based as well as model-based procedures for an improved detection of size and location of the damage. In a first step, Hilbert transform signal processing techniques allow for a computation of the signal envelope and the instantaneous frequency, so that various types of non-linearities due to a damage may be identified and classified based on measured response data. In a second step, a multi-hypothesis bank of Kalman Filters is employed for the detection of the size and location of the damage based on the information of the type of damage provided by the results of the Hilbert transform.
Keywords: Hilbert transform, damage diagnosis, Kalman filtering, non-linear dynamics
(23 pages, 1998)

3. Y. Ben-Haim, S. Seibold

Robust Reliability of Diagnostic Multi-Hypothesis Algorithms: Application to Rotating Machinery

Damage diagnosis based on a bank of Kalman filters, each one conditioned on a specific hypothesized system condition, is a well recognized and powerful diagnostic tool. This multi-hypothesis approach can be applied to a wide range of damage conditions. In this paper, we will focus on the diagnosis of cracks in rotating machinery. The question we address is: how to optimize the multi-hypothesis algorithm with respect to the uncertainty of the spatial form and location of cracks and their resulting dynamic effects. First, we formulate a measure of the reliability of the diagnostic algorithm, and then we discuss modifications of the diagnostic algorithm for the maximization of the reliability. The reliability of a diagnostic algorithm is measured by the amount of uncertainty consistent with no-failure of the diagnosis. Uncertainty is quantitatively represented with convex models.
Keywords: Robust reliability, convex models, Kalman filtering, multi-hypothesis diagnosis, rotating machinery, crack diagnosis
(24 pages, 1998)

4. F.-Th. Lentes, N. Siedow

Three-dimensional Radiative Heat Transfer in Glass Cooling Processes

For the numerical simulation of 3D radiative heat transfer in glasses and glass melts, practically applicable mathematical methods are needed to handle such problems optimal using workstation class computers. Since the exact solution would require super-computer capabilities we concentrate on approximate solutions with a high degree of accuracy. The following approaches are studied: 3D diffusion approximations and 3D ray-tracing methods.
(23 pages, 1998)

5. A. Klar, R. Wegener

A hierarchy of models for multilane vehicular traffic
Part I: Modeling

In the present paper multilane models for vehicular traffic are considered. A microscopic multilane model based on reaction thresholds is developed. Based on this model an Enskog like kinetic model is developed. In particular, care is taken to incorporate the correlations between the vehicles. From the kinetic model a fluid dynamic model is derived. The macroscopic coefficients are deduced from the underlying kinetic model. Numerical simulations are presented for all three levels of description in [10]. Moreover, a comparison of the results is given there.
(23 pages, 1998)

Part II: Numerical and stochastic investigations

In this paper the work presented in [6] is continued. The present paper contains detailed numerical investigations of the models developed there. A numerical method to treat the kinetic equations obtained in [6] are presented and results of the simulations are shown. Moreover, the stochastic correlation model used in [6] is described and investigated in more detail.
(17 pages, 1998)

6. A. Klar, N. Siedow

Boundary Layers and Domain Decomposition for Radiative Heat Transfer and Diffusion Equations: Applications to Glass Manufacturing Processes

In this paper domain decomposition methods for radiative transfer problems including conductive heat transfer are treated. The paper focuses on semi-transparent materials, like glass, and the associated conditions at the interface between the materials. Using asymptotic analysis we derive conditions for the coupling of the radiative transfer equations and a diffusion approximation. Several test cases are treated and a problem appearing in glass manufacturing processes is computed. The results clearly show the advantages of a domain decomposition approach. Accuracy equivalent to the solution of the global radiative transfer solution is achieved, whereas computation time is strongly reduced.
(24 pages, 1998)

7. I. Choquet

Heterogeneous catalysis modelling and numerical simulation in rarified gas flows Part I: Coverage locally at equilibrium

A new approach is proposed to model and simulate numerically heterogeneous catalysis in rarefied gas flows. It is developed to satisfy all together the following points:
1) describe the gas phase at the microscopic scale, as required in rarefied flows,
2) describe the wall at the macroscopic scale, to avoid prohibitive computational costs and consider not only crystalline but also amorphous surfaces,
3) reproduce on average macroscopic laws correlated with experimental results and
4) derive analytic models in a systematic and exact way.
The problem is stated in the general framework of a non static flow in the vicinity of a catalytic and non porous surface (without aging). It is shown that the exact and systematic resolution method based on the Laplace transform, introduced previously by the author to model collisions in the gas phase, can be extended to the present problem. The proposed approach is applied to the modelling of the Eley-Rideal and Langmuir-Hinshelwood recombinations, assuming that the coverage is locally at equilibrium. The models are developed considering one atomic species and extended to the general case of several atomic species. Numerical calculations show that the models derived in this way reproduce with accuracy behaviors observed experimentally.
(24 pages, 1998)

8. J. Ohser, B. Steinbach, C. Lang

Efficient Texture Analysis of Binary Images

A new method of determining some characteristics of binary images is proposed based on a special linear filtering. This technique enables the estimation of the area fraction, the specific line length, and the specific integral of curvature. Furthermore, the specific length of the total projection is obtained, which gives detailed information about the texture of the image. The influence of lateral and directional resolution depending on the size of the applied filter mask is discussed in detail. The technique includes a method of increasing directional resolution for texture analysis while keeping lateral resolution as high as possible.
(17 pages, 1998)

9. J. Orlik

Homogenization for viscoelasticity of the integral type with aging and shrinkage

A multi-phase composite with periodic distributed inclusions with a smooth boundary is considered in this contribution. The composite component materials are supposed to be linear viscoelastic and aging (of the non-convolution integral type, for which the Laplace transform with respect to time is not effectively applicable) and are subjected to isotropic shrinkage. The free shrinkage deformation can be considered as a fictitious temperature deformation in the behavior law. The procedure presented in this paper proposes a way to determine average (effective homogenized) viscoelastic and shrinkage (temperature) composite properties and the homogenized stress-field from known properties of the components. This is done by the extension of the asymptotic homogenization technique known for pure elastic non-homogeneous bodies to the non-homo-

geneous thermo-viscoelasticity of the integral non-convolution type. Up to now, the homogenization theory has not covered viscoelasticity of the integral type. Sanchez-Palencia (1980), Francfort & Suquet (1987) (see [2], [9]) have considered homogenization for viscoelasticity of the differential form and only up to the first derivative order. The integral-modeled viscoelasticity is more general then the differential one and includes almost all known differential models. The homogenization procedure is based on the construction of an asymptotic solution with respect to a period of the composite structure. This reduces the original problem to some auxiliary boundary value problems of elasticity and viscoelasticity on the unit periodic cell, of the same type as the original non-homogeneous problem. The existence and uniqueness results for such problems were obtained for kernels satisfying some constrain conditions. This is done by the extension of the Volterra integral operator theory to the Volterra operators with respect to the time, whose 1 kernels are space linear operators for any fixed time variables. Some ideas of such approach were proposed in [11] and [12], where the Volterra operators with kernels depending additionally on parameter were considered. This manuscript delivers results of the same nature for the case of the space-operator kernels.
(20 pages, 1998)

10. J. Mohring

Helmholtz Resonators with Large Aperture

The lowest resonant frequency of a cavity resonator is usually approximated by the classical Helmholtz formula. However, if the opening is rather large and the front wall is narrow this formula is no longer valid. Here we present a correction which is of third order in the ratio of the diameters of aperture and cavity. In addition to the high accuracy it allows to estimate the damping due to radiation. The result is found by applying the method of matched asymptotic expansions. The correction contains form factors describing the shapes of opening and cavity. They are computed for a number of standard geometries. Results are compared with numerical computations.
(21 pages, 1998)

11. H. W. Hamacher, A. Schöbel

On Center Cycles in Grid Graphs

Finding "good" cycles in graphs is a problem of great interest in graph theory as well as in locational analysis. We show that the center and median problems are NP hard in general graphs. This result holds both for the variable cardinality case (i.e. all cycles of the graph are considered) and the fixed cardinality case (i.e. only cycles with a given cardinality p are feasible). Hence it is of interest to investigate special cases where the problem is solvable in polynomial time. In grid graphs, the variable cardinality case is, for instance, trivially solvable if the shape of the cycle can be chosen freely.
If the shape is fixed to be a rectangle one can analyze rectangles in grid graphs with, in sequence, fixed dimension, fixed cardinality, and variable cardinality. In all cases a complete characterization of the optimal cycles and closed form expressions of the optimal objective values are given, yielding polynomial time algorithms for all cases of center rectangle problems.
Finally, it is shown that center cycles can be chosen as rectangles for small cardinalities such that the center cycle problem in grid graphs is in these cases completely solved.
(15 pages, 1998)

12. H. W. Hamacher, K.-H. Küfer

Inverse radiation therapy planning - a multiple objective optimisation approach

For some decades radiation therapy has been proved successful in cancer treatment. It is the major task of clinical radiation treatment planning to realize on the one hand a high level dose of radiation in the cancer tissue in order to obtain maximum tumor control. On the other hand it is obvious that it is absolutely necessary to keep in the tissue outside the tumor, particularly in organs at risk, the unavoidable radiation as low as possible.
No doubt, these two objectives of treatment planning - high level dose in the tumor, low radiation outside the tumor - have a basically contradictory nature. Therefore, it is no surprise that inverse mathematical models with dose distribution bounds tend to be infeasible in most cases. Thus, there is need for approximations compromising between overdosing the organs at risk and underdosing the target volume.
Differing from the currently used time consuming iterative approach, which measures deviation from an ideal (non-achievable) treatment plan using recursively trial-and-error weights for the organs of interest, we go a new way trying to avoid a priori weight choices and consider the treatment planning problem as a multiple objective linear programming problem: with each organ of interest, target tissue as well as organs at risk, we associate an objective function measuring the maximal deviation from the prescribed doses.
We build up a data base of relatively few efficient solutions representing and approximating the variety of Pareto solutions of the multiple objective linear programming problem. This data base can be easily scanned by physicians looking for an adequate treatment plan with the aid of an appropriate online tool.
(14 pages, 1999)

13. C. Lang, J. Ohser, R. Hilfer

On the Analysis of Spatial Binary Images

This paper deals with the characterization of microscopically heterogeneous, but macroscopically homogeneous spatial structures. A new method is presented which is strictly based on integral-geometric formulae such as Crofton's intersection formulae and Hadwiger's recursive definition of the Euler number. The corresponding algorithms have clear advantages over other techniques. As an example of application we consider the analysis of spatial digital images produced by means of Computer Assisted Tomography.
(20 pages, 1999)

14. M. Junk

On the Construction of Discrete Equilibrium Distributions for Kinetic Schemes

A general approach to the construction of discrete equilibrium distributions is presented. Such distribution functions can be used to set up Kinetic Schemes as well as Lattice Boltzmann methods. The general principles are also applied to the construction of Chapman Enskog distributions which are used in Kinetic Schemes for compressible Navier-Stokes equations.
(24 pages, 1999)

15. M. Junk, S. V. Raghurame Rao

A new discrete velocity method for Navier-Stokes equations

The relation between the Lattice Boltzmann Method, which has recently become popular, and the Kinetic Schemes, which are routinely used in Computational Fluid Dynamics, is explored. A new discrete velocity model for the numerical solution of Navier-Stokes equations for incompressible fluid flow is presented by combining both the approaches. The new scheme can be interpreted as a pseudo-compressibility method and, for a particular choice of parameters, this interpretation carries over to the Lattice Boltzmann Method.
(20 pages, 1999)

16. H. Neunzert

Mathematics as a Key to Key Technologies

The main part of this paper will consist of examples, how mathematics really helps to solve industrial problems; these examples are taken from our Institute for Industrial Mathematics, from research in the Technomathematics group at my university, but also from ECMI groups and a company called TecMath, which originated 10 years ago from my university group and has already a very successful history.
(39 pages (4 PDF-Files), 1999)

17. J. Ohser, K. Sandau

Considerations about the Estimation of the Size Distribution in Wicksell's Corpuscle Problem

Wicksell's corpuscle problem deals with the estimation of the size distribution of a population of particles, all having the same shape, using a lower dimensional sampling probe. This problem was originary formulated for particle systems occurring in life sciences but its solution is of actual and increasing interest in materials science. From a mathematical point of view, Wicksell's problem is an inverse problem where the interesting size distribution is the unknown part of a Volterra equation. The problem is often regarded ill-posed, because the structure of the integrand implies unstable numerical solutions. The accuracy of the numerical solutions is considered here using the condition number, which allows to compare different numerical methods with different (equidistant) class sizes and which indicates, as one result, that a finite section thickness of the probe reduces the numerical problems. Furthermore, the relative error of estimation is computed which can be split into two parts. One part consists of the relative discretization error that increases for increasing class size, and the second part is related to the relative statistical error which increases with decreasing class size. For both parts, upper bounds can be given and the sum of them indicates an optimal class width depending on some specific constants.
(18 pages, 1999)

18. E. Carrizosa, H. W. Hamacher, R. Klein, S. Nickel

Solving nonconvex planar location problems by finite dominating sets

It is well-known that some of the classical location problems with polyhedral gauges can be solved in polynomial time by finding a finite dominating set, i. e. a finite set

of candidates guaranteed to contain at least one optimal location.
In this paper it is first established that this result holds for a much larger class of problems than currently considered in the literature. The model for which this result can be proven includes, for instance, location problems with attraction and repulsion, and location-allocation problems. Next, it is shown that the approximation of general gauges by polyhedral ones in the objective function of our general model can be analyzed with regard to the subsequent error in the optimal objective value. For the approximation problem two different approaches are described, the sandwich procedure and the greedy algorithm. Both of these approaches lead - for fixed epsilon - to polynomial approximation algorithms with accuracy epsilon for solving the general model considered in this paper.
Keywords: Continuous Location, Polyhedral Gauges, Finite Dominating Sets, Approximation, Sandwich Algorithm, Greedy Algorithm
(19 pages, 2000)

19. A. Becker

A Review on Image Distortion Measures

Within this paper we review image distortion measures. A distortion measure is a criterion that assigns a "quality number" to an image. We distinguish between mathematical distortion measures and those distortion measures in-cooperating a priori knowledge about the imaging devices (e. g. satellite images), image processing algorithms or the human physiology. We will consider representative examples of different kinds of distortion measures and are going to discuss them.
Keywords: Distortion measure, human visual system
(26 pages, 2000)

20. H. W. Hamacher, M. Labbé, S. Nickel, T. Sonneborn

Polyhedral Properties of the Uncapacitated Multiple Allocation Hub Location Problem

We examine the feasibility polyhedron of the uncapacitated hub location problem (UHL) with multiple allocation, which has applications in the fields of air passenger and cargo transportation, telecommunication and postal delivery services. In particular we determine the dimension and derive some classes of facets of this polyhedron. We develop some general rules about lifting facets from the uncapacitated facility location (UFL) for UHL and projecting facets from UHL to UFL. By applying these rules we get a new class of facets for UHL which dominates the inequalities in the original formulation. Thus we get a new formulation of UHL whose constraints are all facet–defining. We show its superior computational performance by benchmarking it on a well known data set.
Keywords: integer programming, hub location, facility location, valid inequalities, facets, branch and cut
(21 pages, 2000)

21. H. W. Hamacher, A. Schöbel

Design of Zone Tariff Systems in Public Transportation

Given a public transportation system represented by its stops and direct connections between stops, we consider two problems dealing with the prices for the customers: The fare problem in which subsets of stops are already aggregated to zones and "good" tariffs have to be found in the existing zone system. Closed form solutions for the fare problem are presented for three objective functions. In the zone problem the design of the zones is part of the problem. This problem is NP hard and we therefore propose three heuristics which prove to be very successful in the redesign of one of Germany's transportation systems.
(30 pages, 2001)

22. D. Hietel, M. Junk, R. Keck, D. Teleaga:

The Finite-Volume-Particle Method for Conservation Laws

In the Finite-Volume-Particle Method (FVPM), the weak formulation of a hyperbolic conservation law is discretized by restricting it to a discrete set of test functions. In contrast to the usual Finite-Volume approach, the test functions are not taken as characteristic functions of the control volumes in a spatial grid, but are chosen from a partition of unity with smooth and overlapping partition functions (the particles), which can even move along prescribed velocity fields. The information exchange between particles is based on standard numerical flux functions. Geometrical information, similar to the surface area of the cell faces in the Finite-Volume Method and the corresponding normal directions are given as integral quantities of the partition functions. After a brief derivation of the Finite-Volume-Particle Method, this work focuses on the role of the geometric coefficients in the scheme.
(16 pages, 2001)

23. T. Bender, H. Hennes, J. Kalcsics, M. T. Melo, S. Nickel

Location Software and Interface with GIS and Supply Chain Management

The objective of this paper is to bridge the gap between location theory and practice. To meet this objective focus is given to the development of software capable of addressing the different needs of a wide group of users. There is a very active community on location theory encompassing many research fields such as operations research, computer science, mathematics, engineering, geography, economics and marketing. As a result, people working on facility location problems have a very diverse background and also different needs regarding the software to solve these problems. For those interested in non-commercial applications (e. g. students and researchers), the library of location algorithms (LoLA can be of considerable assistance. LoLA contains a collection of efficient algorithms for solving planar, network and discrete facility location problems. In this paper, a detailed description of the functionality of LoLA is presented. In the fields of geography and marketing, for instance, solving facility location problems requires using large amounts of demographic data. Hence, members of these groups (e. g. urban planners and sales managers) often work with geographical information too s. To address the specific needs of these users, LoLA was inked to a geographical information system (GIS) and the details of the combined functionality are described in the paper. Finally, there is a wide group of practitioners who need to solve large problems and require special purpose software with a good data interface. Many of such users can be found, for example, in the area of supply chain management (SCM). Logistics activities involved in strategic SCM include, among others, facility location planning. In this paper, the development of a commercial location software tool is also described. The too is embedded in the Advanced Planner and Optimizer SCM software developed by SAP AG, Walldorf, Germany. The paper ends with some conclusions and an outlook to future activities.
Keywords: facility location, software development, geographical information systems, supply chain management.
(48 pages, 2001)

24. H. W. Hamacher, S. A. Tjandra

Mathematical Modelling of Evacuation Problems: A State of Art

This paper details models and algorithms which can be applied to evacuation problems. While it concentrates on building evacuation many of the results are applicable also to regional evacuation. All models consider the time as main parameter, where the travel time between components of the building is part of the input and the overall evacuation time is the output. The paper distinguishes between macroscopic and microscopic evacuation models both of which are able to capture the evacuees' movement over time.
Macroscopic models are mainly used to produce good lower bounds for the evacuation time and do not consider any individual behavior during the emergency situation. These bounds can be used to analyze existing buildings or help in the design phase of planning a building. Macroscopic approaches which are based on dynamic network flow models (minimum cost dynamic flow, maximum dynamic flow, universal maximum flow, quickest path and quickest flow) are described. A special feature of the presented approach is the fact, that travel times of evacuees are not restricted to be constant, but may be density dependent. Using multicriteria optimization priority regions and blockage due to fire or smoke may be considered. It is shown how the modelling can be done using time parameter either as discrete or continuous parameter.
Microscopic models are able to model the individual evacuee's characteristics and the interaction among evacuees which influence their movement. Due to the corresponding huge amount of data one uses simulation approaches. Some probabilistic laws for individual evacuee's movement are presented. Moreover ideas to model the evacuee's movement using cellular automata (CA) and resulting software are presented.
In this paper we will focus on macroscopic models and only summarize some of the results of the microscopic approach. While most of the results are applicable to general evacuation situations, we concentrate on building evacuation.
(44 pages, 2001)

25. J. Kuhnert, S. Tiwari

Grid free method for solving the Poisson equation

A Grid free method for solving the Poisson equation is presented. This is an iterative method. The method is based on the weighted least squares approximation in which the Poisson equation is enforced to be satisfied in every iterations. The boundary conditions can also be enforced in the iteration process. This is a local approximation procedure. The Dirichlet, Neumann and mixed boundary value problems on a unit square are presented and the analytical solutions are compared with the exact solutions. Both solutions matched perfectly.
Keywords: Poisson equation, Least squares method, Grid free method
(19 pages, 2001)

26. T. Götz, H. Rave, D. Reinel-Bitzer, K. Steiner, H. Tiemeier

Simulation of the fiber spinning process

To simulate the influence of process parameters to the melt spinning process a fiber model is used and coupled with CFD calculations of the quench air flow. In the fiber model energy, momentum and mass balance are solved for the polymer mass flow. To calculate the quench air the Lattice Boltzmann method is used. Simulations and experiments for different process parameters and hole configurations are compared and show a good agreement.
Keywords: Melt spinning, fiber model, Lattice Boltzmann, CFD
(19 pages, 2001)

27. A. Zemitis

On interaction of a liquid film with an obstacle

In this paper mathematical models for liquid films generated by impinging jets are discussed. Attention is stressed to the interaction of the liquid film with some obstacle. S. G. Taylor [Proc. R. Soc. London Ser. A 253, 313 (1959)] found that the liquid film generated by impinging jets is very sensitive to properties of the wire which was used as an obstacle. The aim of this presentation is to propose a modification of the Taylor's model, which allows to simulate the film shape in cases, when the angle between jets is different from 180°. Numerical results obtained by discussed models give two different shapes of the liquid film similar as in Taylors experiments. These two shapes depend on the regime: either droplets are produced close to the obstacle or not. The difference between two regimes becomes larger if the angle between jets decreases. Existence of such two regimes can be very essential for some applications of impinging jets, if the generated liquid film can have a contact with obstacles.
Keywords: impinging jets, liquid film, models, numerical solution, shape
(22 pages, 2001)

28. I. Ginzburg, K. Steiner

Free surface lattice-Boltzmann method to model the filling of expanding cavities by Bingham Fluids

The filling process of viscoplastic metal alloys and plastics in expanding cavities is modelled using the lattice Boltzmann method in two and three dimensions. These models combine the regularized Bingham model for viscoplastic with a free-interface algorithm. The latter is based on a modified immiscible lattice Boltzmann model in which one species is the fluid and the other one is considered as vacuum. The boundary conditions at the curved liquid-vacuum interface are met without any geometrical front reconstruction from a first-order Chapman-Enskog expansion. The numerical results obtained with these models are found in good agreement with available theoretical and numerical analysis.
Keywords: Generalized LBE, free-surface phenomena, interface boundary conditions, filling processes, Bingham viscoplastic model, regularized models
(22 pages, 2001)

29. H. Neunzert

»Denn nichts ist für den Menschen als Menschen etwas wert, was er nicht mit Leidenschaft tun kann«

Vortrag anlässlich der Verleihung des Akademiepreises des Landes Rheinland-Pfalz am 21.11.2001

Was macht einen guten Hochschullehrer aus? Auf diese Frage gibt es sicher viele verschiedene, fachbezogene Antworten, aber auch ein paar allgemeine Gesichtspunkte: es bedarf der »Leidenschaft« für die Forschung (Max Weber), aus der dann auch die Begeisterung für die Lehre erwächst. Forschung und Lehre gehören zusammen, um die Wissenschaft als lebendiges Tun vermitteln zu können. Der Vortrag gibt Beispiele dafür, wie in angewandter Mathematik Forschungsaufgaben aus praktischen Alltagsproblemstellungen erwachsen, die in die Lehre auf verschiedenen Stufen (Gymnasium bis Graduiertenkolleg) einfließen; er leitet damit auch zu einem aktuellen Forschungsgebiet, der Mehrskalenanalyse mit ihren vielfältigen Anwendungen in Bildverarbeitung, Materialentwicklung und Strömungsmechanik über, was aber nur kurz gestreift wird. Mathematik erscheint hier als eine moderne Schlüsseltechnologie, die aber auch enge Beziehungen zu den Geistes- und Sozialwissenschaften hat.
Keywords: Lehre, Forschung, angewandte Mathematik, Mehrskalenanalyse, Strömungsmechanik
(18 pages, 2001)

30. J. Kuhnert, S. Tiwari

Finite pointset method based on the projection method for simulations of the incompressible Navier-Stokes equations

A Lagrangian particle scheme is applied to the projection method for the incompressible Navier-Stokes equations. The approximation of spatial derivatives is obtained by the weighted least squares method. The pressure Poisson equation is solved by a local iterative procedure with the help of the least squares method. Numerical tests are performed for two dimensional cases. The Couette flow, Poiseuelle flow, decaying shear flow and the driven cavity flow are presented. The numerical solutions are obtained for stationary as well as instationary cases and are compared with the analytical solutions for channel flows. Finally, the driven cavity in a unit square is considered and the stationary solution obtained from this scheme is compared with that from the finite element method.
Keywords: Incompressible Navier-Stokes equations, Meshfree method, Projection method, Particle scheme, Least squares approximation
AMS subject classification: 76D05, 76M28
(25 pages, 2001)

31. R. Korn, M. Krekel

Optimal Portfolios with Fixed Consumption or Income Streams

We consider some portfolio optimisation problems where either the investor has a desire for an a priori specified consumption stream or/and follows a deterministic pay in scheme while also trying to maximize expected utility from final wealth. We derive explicit closed form solutions for continuous and discrete monetary streams. The mathematical method used is classical stochastic control theory.
Keywords: Portfolio optimisation, stochastic control, HJB equation, discretisation of control problems.
(23 pages, 2002)

32. M. Krekel

Optimal portfolios with a loan dependent credit spread

If an investor borrows money he generally has to pay higher interest rates than he would have received, if he had put his funds on a savings account. The classical model of continuous time portfolio optimisation ignores this effect. Since there is obviously a connection between the default probability and the total percentage of wealth, which the investor is in debt, we study portfolio optimisation with a control dependent interest rate. Assuming a logarithmic and a power utility function, respectively, we prove explicit formulae of the optimal control.
Keywords: Portfolio optimisation, stochastic control, HJB equation, credit spread, log utility, power utility, nonlinear wealth dynamics
(25 pages, 2002)

33. J. Ohser, W. Nagel, K. Schladitz

The Euler number of discretized sets - on the choice of adjacency in homogeneous lattices

Two approaches for determining the Euler-Poincaré characteristic of a set observed on lattice points are considered in the context of image analysis { the integral geometric and the polyhedral approach. Information about the set is assumed to be available on lattice points only. In order to retain properties of the Euler number and to provide a good approximation of the true Euler number of the original set in the Euclidean space, the appropriate choice of adjacency in the lattice for the set and its background is crucial. Adjacencies are defined using tessellations of the whole space into polyhedrons. In R 3 , two new 14 adjacencies are introduced additionally to the well known 6 and 26 adjacencies. For the Euler number of a set and its complement, a consistency relation holds. Each of the pairs of adjacencies (14:1; 14:1), (14:2; 14:2), (6; 26), and (26; 6) is shown to be a pair of complementary adjacencies with respect to this relation. That is, the approximations of the Euler numbers are consistent if the set and its background (complement) are equipped with this pair of adjacencies. Furthermore, sufficient conditions for the correctness of the approximations of the Euler number are given. The analysis of selected microstructures and a simulation study illustrate how the estimated Euler number depends on the chosen adjacency. It also shows that there is not a uniquely best pair of adjacencies with respect to the estimation of the Euler number of a set in Euclidean space.
Keywords: image analysis, Euler number, neighborhod relationships, cuboidal lattice
(32 pages, 2002)

34. I. Ginzburg, K. Steiner

Lattice Boltzmann Model for Free-Surface flow and Its Application to Filling Process in Casting

A generalized lattice Boltzmann model to simulate free-surface is constructed in both two and three dimensions. The proposed model satisfies the interfacial boundary conditions accurately. A distinctive feature of the model is that the collision processes is carried out

only on the points occupied partially or fully by the fluid. To maintain a sharp interfacial front, the method includes an anti-diffusion algorithm. The unknown distribution functions at the interfacial region are constructed according to the first order Chapman-Enskog analysis. The interfacial boundary conditions are satisfied exactly by the coefficients in the Chapman-Enskog expansion. The distribution functions are naturally expressed in the local interfacial coordinates. The macroscopic quantities at the interface are extracted from the least-square solutions of a locally linearized system obtained from the known distribution functions. The proposed method does not require any geometric front construction and is robust for any interfacial topology. Simulation results of realistic filling process are presented: rectangular cavity in two dimensions and Hammer box, Campbell box, Sheffield box, and Motorblock in three dimensions. To enhance the stability at high Reynolds numbers, various upwind-type schemes are developed. Free-slip and no-slip boundary conditions are also discussed.
Keywords: Lattice Boltzmann models; free-surface phenomena; interface boundary conditions; filling processes; injection molding; volume of fluid method; interface boundary conditions; advection-schemes; upwind-schemes
(54 pages, 2002)

35. M. Günther, A. Klar, T. Materne, R. Wegener
Multivalued fundamental diagrams and stop and go waves for continuum traffic equations

In the present paper a kinetic model for vehicular traffic leading to multivalued fundamental diagrams is developed and investigated in detail. For this model phase transitions can appear depending on the local density and velocity of the flow. A derivation of associated macroscopic traffic equations from the kinetic equation is given. Moreover, numerical experiments show the appearance of stop and go waves for highway traffic with a bottleneck.
Keywords: traffic flow, macroscopic equations, kinetic derivation, multivalued fundamental diagram, stop and go waves, phase transitions
(25 pages, 2002)

36. S. Feldmann, P. Lang, D. Prätzel-Wolters
Parameter influence on the zeros of network determinants

To a network N(q) with determinant D(s;q) depending on a parameter vector $q \in R^r$ via identification of some of its vertices, a network $N^\wedge(q)$ is assigned. The paper deals with procedures to find $N^\wedge(q)$, such that its determinant $D^\wedge(s;q)$ admits a factorization in the determinants of appropriate subnetworks, and with the estimation of the deviation of the zeros of $D^\wedge$ from the zeros of D. To solve the estimation problem state space methods are applied.
Keywords: Networks, Equicofactor matrix polynomials, Realization theory, Matrix perturbation theory
(30 pages, 2002)

37. K. Koch, J. Ohser, K. Schladitz
Spectral theory for random closed sets and estimating the covariance via frequency space

A spectral theory for stationary random closed sets is developed and provided with a sound mathematical basis. Definition and proof of existence of the Bartlett spectrum of a stationary random closed set as well as the proof of a Wiener-Khintchine theorem for the power spectrum are used to two ends: First, well known second order characteristics like the covariance can be estimated faster than usual via frequency space. Second, the Bartlett spectrum and the power spectrum can be used as second order characteristics in frequency space. Examples show, that in some cases information about the random closed set is easier to obtain from these characteristics in frequency space than from their real world counterparts.
Keywords: Random set, Bartlett spectrum, fast Fourier transform, power spectrum
(28 pages, 2002)

38. D. d'Humières, I. Ginzburg
Multi-reflection boundary conditions for lattice Boltzmann models

We present a unified approach of several boundary conditions for lattice Boltzmann models. Its general framework is a generalization of previously introduced schemes such as the bounce-back rule, linear or quadratic interpolations, etc. The objectives are two fold: first to give theoretical tools to study the existing boundary conditions and their corresponding accuracy; secondly to design formally third- order accurate boundary conditions for general flows. Using these boundary conditions, Couette and Poiseuille flows are exact solution of the lattice Boltzmann models for a Reynolds number $Re = 0$ (Stokes limit).
Numerical comparisons are given for Stokes flows in periodic arrays of spheres and cylinders, linear periodic array of cylinders between moving plates and for Navier-Stokes flows in periodic arrays of cylinders for $Re < 200$. These results show a significant improvement of the overall accuracy when using the linear interpolations instead of the bounce-back reflection (up to an order of magnitude on the hydrodynamics fields). Further improvement is achieved with the new multi-reflection boundary conditions, reaching a level of accuracy close to the quasi-analytical reference solutions, even for rather modest grid resolutions and few points in the narrowest channels. More important, the pressure and velocity fields in the vicinity of the obstacles are much smoother with multi-reflection than with the other boundary conditions.
Finally the good stability of these schemes is highlighted by some simulations of moving obstacles: a cylinder between flat walls and a sphere in a cylinder.
Keywords: lattice Boltzmann equation, boudary condistions, bounce-back rule, Navier-Stokes equation
(72 pages, 2002)